

¹
² Susceptible host dynamics explain pathogen resilience to
³ perturbations

⁴
⁵ Sang Woo Park^{1,*} Bjarke Frost Nielsen² Emily Howerton² Bryan T. Grenfell^{2,3,4}
⁶ Sarah Cobey¹

⁷ **1** Department of Ecology and Evolution, University of Chicago, Chicago, IL, USA

⁸ **2** Department of Ecology and Evolutionary Biology, Princeton University,
Princeton, NJ, USA

¹⁰ **3** High Meadows Environmental Institute, Princeton University, Princeton, NJ,
USA

¹² **4** Princeton School of Public and International Affairs, Princeton, NJ, USA

¹³ *Corresponding author: swp2@uchicago.edu

¹⁴ **Abstract**

¹⁵ Interventions to slow the spread of SARS-CoV-2 significantly disrupted the transmission
¹⁶ of other pathogens. As interventions lifted, whether and when human pathogens
¹⁷ would eventually return to their pre-pandemic dynamics remains to be answered.
¹⁸ Here, we present a framework for estimating pathogen resilience based on how fast
¹⁹ epidemic patterns return to their pre-pandemic dynamics. By analyzing time series
²⁰ data from Hong Kong, Canada, Korea, and the US, we quantify the resilience of com-
²¹ mon respiratory pathogens and further predict when each pathogen will eventually
²² return to its pre-pandemic dynamics. Our predictions closely match the observed
²³ deviations (or lack thereof) from the pre-COVID dynamics and reveal long-term
²⁴ impacts of pandemic perturbations. We find a faster rate of susceptible replenish-
²⁵ ment underlies pathogen resilience and sensitivity to both large and small perturba-
²⁶ tions. Overall, our analysis highlights the persistent nature of common respiratory
²⁷ pathogens compared to vaccine-preventable infections, such as measles.

Introduction

Non-pharmaceutical interventions to slow the spread of SARS-CoV-2 disrupted the transmission of other human respiratory pathogens, adding uncertainties to their future epidemic dynamics and their public health burden [1]. As interventions lifted, large heterogeneities in outbreak dynamics were observed across different pathogens in different countries, with some pathogens exhibiting earlier and faster resurgences than others [2, 3, 4]. Heterogeneities in the overall reduction in transmission and the timing of re-emergence likely reflect differences in intervention patterns, pathogen characteristics, immigration/importation from other countries, and pre-pandemic pathogen dynamics [5]. Therefore, comparing the differential impact of the pandemic perturbations across pathogens can provide unique opportunities to learn about underlying pathogen characteristics across different populations, such as their transmissibility or duration of immunity, from heterogeneities in re-emergence patterns [6].

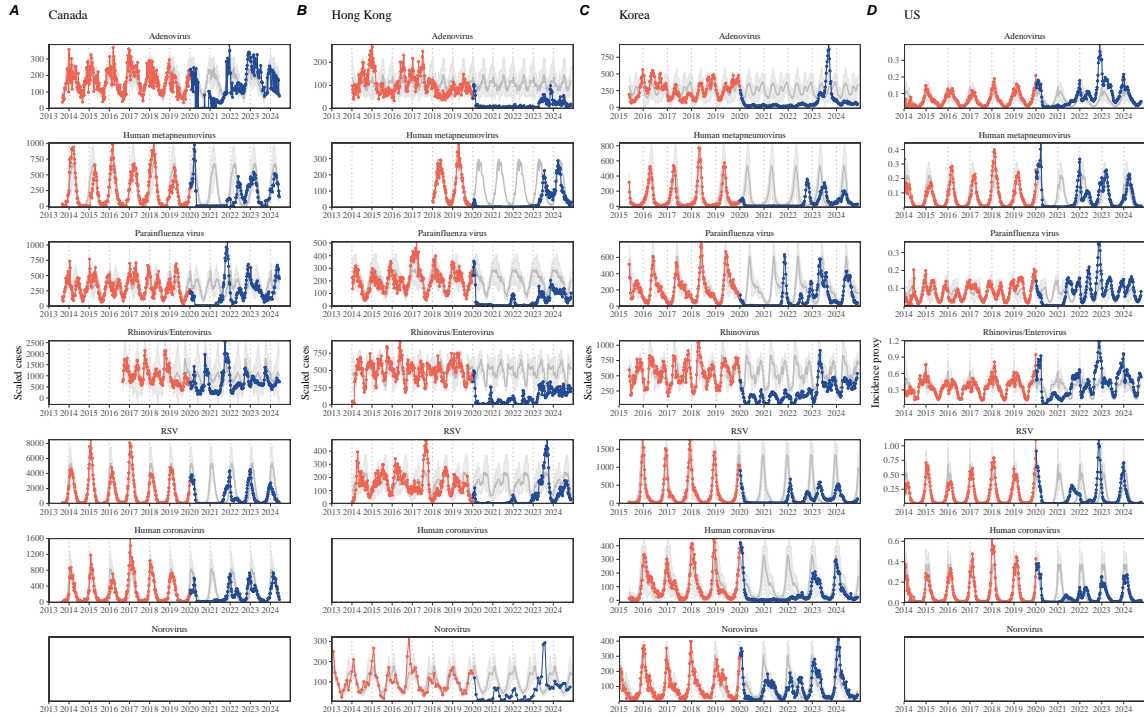


Figure 1: Observed heterogeneity in responses to pandemic perturbations across respiratory pathogens and norovirus in (A) Canada, (B) Hong Kong, (C) Korea, and (D) US. Red points and lines represent data before 2020. Blue points and lines represent data since 2020. Gray lines and shaded regions represent the mean seasonal patterns and corresponding 95% confidence intervals around the mean. Mean seasonal patterns were calculated by aggregating cases before 2020 into 52 weekly bins and taking the average in each week. Cases were scaled to account for changes in testing patterns (Materials and Methods).

42 Even though more than five years have passed since the emergence of SARS-CoV-
43 2, we still observe persistent changes in pathogen dynamics following the pandemic
44 perturbations. For example, compared to pre-pandemic, seasonal patterns, human
45 metapneumovirus in Korea seems to circulate at lower levels, whereas RSV in Ko-
46 rea seems to exhibit different seasonality (Figure 1). These observations suggest
47 the possibility of a long-term change in pathogen dynamics following the pandemic
48 perturbations, which might be driven by a long-term shift in human behavior or
49 population-level immunity [7, 8]. For example, the emergence of SARS-CoV-2 could
50 have caused a long-term shift in population-level immunity through its interactions
51 with other pathogens [9], especially with seasonal coronaviruses [7, 10, 11]. The pos-
52 sibility of a long-lasting impact of the pandemic perturbations poses an important
53 question for future infectious disease dynamics: can we predict whether and when
54 other pathogens will eventually return to their pre-pandemic dynamics?

55 So far, most analyses of respiratory pathogens after pandemic perturbations have
56 focused on characterizing the timing of rebound [1, 12, 5]. Instead, we seek to char-
57 acterize how fast (and whether) a pathogen returns to its pre-pandemic dynamics.
58 These two concepts have a subtle but important difference. For example, it took
59 more than 3 years for human metapneumovirus to rebound in Hong Kong, but the
60 observed epidemic patterns in 2024 appear similar to the pre-pandemic seasonal
61 mean, suggesting a possible return to pre-pandemic dynamics, though confirmation
62 may require multiple seasons (Figure 1). Measuring this rate of return is useful be-
63 cause it allows us to quantify the ecological resilience of a host-pathogen system,
64 which can inform responses to future interventions [13, 14, 15, 16].

65 In this study, we lay out theoretical and statistical approaches to characterizing
66 the resilience of a host-pathogen system based on how fast the system recovers from
67 perturbation. We begin by laying out a few representative scenarios that capture
68 the potential impact of pandemic perturbations on endemic pathogen dynamics and
69 illustrate how resilience can be measured by comparing the pre- and post-pandemic
70 dynamics of susceptible and infected hosts. In practice, information on susceptible
71 hosts is often unavailable, making this theoretical approach infeasible. Instead, we
72 utilize a mathematical technique to reconstruct attractors from the data [17], which
73 allows us to measure the rate at which the host-pathogen system approaches this
74 empirical attractor after a perturbation; we define this rate to be the empirical
75 resilience of the host-pathogen system. We use this method to analyze pathogen
76 surveillance data for respiratory and non-respiratory pathogens from Canada, Hong
77 Kong, Korea, and the US. Finally, we show that susceptible host dynamics explain
78 variation in pathogen resilience and demonstrate that more resilient pathogens will be
79 less sensitive to perturbations caused by demographic stochasticity, thereby providing
80 a direct link between pathogen resilience and persistence.

⁸¹ Conceptual introduction to pathogen resilience

⁸² In the classical ecological literature, the resilience of an ecological system is measured
⁸³ by the rate at which the system returns to its reference state following a perturbation
⁸⁴ [13, 14, 15, 16]. This rate corresponds to the largest real part of the eigenvalues of
⁸⁵ the linearized system near equilibrium—here, we refer to this value as the *intrinsic*
⁸⁶ resilience of the system, which represents the expected rate of return from perturbed
⁸⁷ states. In practice, we rarely know the true model describing the dynamics of com-
⁸⁸ mon respiratory pathogens, limiting our ability to infer the intrinsic resilience of a
⁸⁹ system. Instead, we can measure the *empirical* resilience of a host-pathogen system
⁹⁰ by looking at how fast the system returns to the pre-perturbation endemic dynamics
⁹¹ after the perturbation has ended. The COVID-19 pandemic provides a crucial exam-
⁹² ple of a major perturbation, providing unique opportunities to measure the resilience
⁹³ of a host-pathogen system across different countries.

⁹⁴ **Resilience of a single-strain system under a short-term perturbation.**
⁹⁵ As an example, we begin with a simple Susceptible-Infected-Recovered-Susceptible
⁹⁶ (SIRS) model with seasonally forced transmission and demography (i.e., birth and
⁹⁷ death). The SIRS model is the simplest model that allows for the waning of immunity
⁹⁸ and is commonly used for modeling the dynamics of respiratory pathogens [18]. First,
⁹⁹ consider a pandemic perturbation that reduces transmission by 50% for 6 months
¹⁰⁰ starting in 2020, which causes epidemic patterns to deviate from their original stable
¹⁰¹ annual cycle for a short period of time and eventually come back (Figure 2A). To
¹⁰² measure the resilience of this system empirically, we first need to be able to measure
¹⁰³ the distance from its pre-pandemic attractor, which is defined as a set of points in
¹⁰⁴ state space or phase plane that the system is pulled towards [19]. There are many
¹⁰⁵ ways we can measure the distance from the attractor, but for illustrative purposes, we
¹⁰⁶ choose one of the most parsimonious approaches: we look at how the susceptible (S)
¹⁰⁷ and infected (I) populations change over time and measure the Euclidean distance on
¹⁰⁸ the SI phase plane, using the counterfactual unperturbed phase plane as a reference
¹⁰⁹ (Figure 2B; Materials and Methods). In this simple case, the locally estimated
¹¹⁰ scatterplot smoothing (LOESS) fit indicates that the distance from the attractor
¹¹¹ decreases exponentially (linearly on a log scale) with time on average (Figure 2C).
¹¹² Furthermore, the overall rate of return approximates the intrinsic resilience of the
¹¹³ seasonally unforced system (Figure 2C).

¹¹⁴ **Resilience of a single-strain system under a long-term perturbation.**
¹¹⁵ Alternatively, pandemic perturbations can have a lasting impact on the forces driv-
¹¹⁶ ing pathogen dynamics through a long-term reduction in transmission or permanent
¹¹⁷ change in immunity. As an example, we consider a scenario in which a 10% reduc-
¹¹⁸ tion in transmission persists even after the major pandemic perturbations are lifted
¹¹⁹ (Figure 2D–F). In such cases, we cannot know whether the pathogen will return to
¹²⁰ its original cycle or a different cycle until many years have passed, and we cannot
¹²¹ a priori measure the distance to the new unknown attractor that the system might
¹²² eventually approach. Nonetheless, we can still measure the distance from the pre-

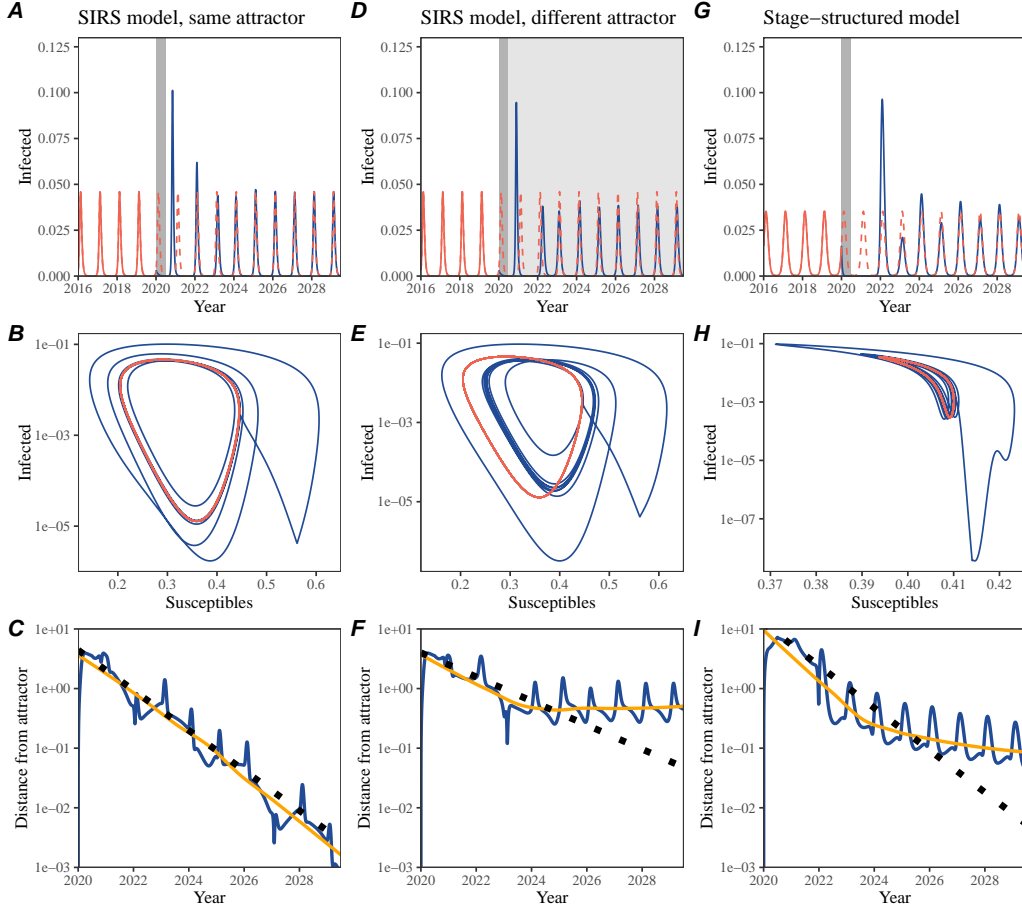


Figure 2: A simple method to measure pathogen resilience following pandemic perturbations across different scenarios. (A, D, G) Simulated epidemic trajectories across various models. Red and blue solid lines represent epidemic dynamics before and after pandemic perturbations are introduced, respectively. Red dashed lines represent counterfactual epidemic dynamics in the absence of perturbations. Gray regions indicate the duration of perturbations with the dark gray region representing a 50% transmission reduction and the light gray region representing a 10% transmission reduction. (B, E, H) Phase plane representation of the time series in panels A, D, and G alongside the corresponding susceptible host dynamics. Red and blue solid lines represent epidemic trajectories on an SI phase plane before and after perturbations are introduced, respectively. (C, F, I) Changes in distance from the attractor over time on a log scale. Blue lines represent the distance from the attractor. Orange lines represent the locally estimated scatterplot smoothing (LOESS) fits to the logged distance from the attractor. Dotted lines show the intrinsic resilience of the seasonally unforced system.

123 pandemic attractor and ask how the distance changes over time (Figure 2E). The
124 LOESS fit suggests that the distance from the pre-pandemic attractor will initially
125 decrease exponentially on average (equivalently, linearly on a log scale) and even-
126 tually plateau (Figure 2F). Here, a permanent 10% reduction in transmission rate
127 slows the system, which causes the distance from the pre-pandemic attractor initially
128 to decrease at a slower rate (Figure 2F) than it would have otherwise (Figure 2C)
129 before plateauing at a fixed distance between the two attractors. This example shows
130 that resilience is not necessarily an intrinsic property of a specific pathogen. Instead,
131 pathogen resilience is a property of a specific attractor that a host-pathogen system
132 approaches, which depends on both pathogen and host characteristics.

133 **Resilience of a single-strain system with long-term transients.** Finally,
134 transient phenomena can further complicate the picture (Figure 2G–I). For exam-
135 ple, a stage-structured model that accounts for reduction in secondary susceptibility
136 initially exhibits a stable annual cycle, but perturbations from a 10% reduction in
137 transmission for 6 months cause the epidemic to shift to biennial cycles (Figure 2G).
138 The system eventually approaches the original pre-pandemic attractor (Figure 2H),
139 suggesting that this biennial cycle is a transient. The LOESS fit indicates that the
140 distance from the attractor initially decreases exponentially at a rate that is consis-
141 tent with the intrinsic resilience of the seasonally unforced stage-structured system,
142 but the approach to the attractor slows down with the damped oscillations (Figure
143 2I). This behavior is also referred to as a ghost attractor, which causes long tran-
144 sient dynamics and slow transitions [20]. Strong seasonal forcing in transmission can
145 also lead to transient phenomena for a simple SIRS model, causing a slow return to
146 pre-perturbation dynamics (Supplementary Figure S1).

147 **Resilience of a two-strain system.** This empirical approach allows us to
148 measure the resilience of a two-strain host-pathogen system as well even when we
149 have incomplete observation of the infection dynamics. Simulations from a simple
150 two-strain competition system illustrate that separate analyses of individual strain
151 dynamics (e.g., RSV subtype A vs B) and a joint analysis of total infections (e.g.,
152 total RSV infections) yield identical resilience estimates (Supplementary Figure S2,
153 3). This is expected because eigenvalues determine the dynamics of the entire system
154 around the equilibrium, meaning that both strains should exhibit identical rates of
155 return following a perturbation. Analogous to a single-strain system, strong sea-
156 sonal forcing in transmission can cause the two-strain system to slow down through
157 transient phenomena (Supplementary Figure S4).

158 These observations yield three insights. First, we can directly estimate the empi-
159 rical resilience of a host-pathogen system by measuring the rate at which the system
160 approaches an attractor, provided that we have a way to quantify the distance from
161 the attractor—as we discuss later, the attractor of a system can be reconstructed
162 from data from mathematical theory without making assumptions about the under-
163 lying model. The empirical approach to estimating pathogen resilience is particularly
164 convenient because it does not require us to know the true underlying model; esti-
165 mating the intrinsic resilience from fitting misspecified models can lead to biased

estimates (Supplementary Figure S5). Second, resilience estimates allow us to make phenomenological predictions about the dynamics of a host-pathogen system following a perturbation. Assuming that an attractor has not changed and the distance from the attractor will decrease exponentially over time, we can estimate when the system should reach an attractor. Finally, a change in the (exponential) rate of approach can provide information about whether the system has reached an alternative attractor, or a ghost attractor, that is different from the original, pre-pandemic attractor. These alternative attractors may reflect permanent changes in transmission patterns as well as changes in immune landscapes. There will be periods of time when it is difficult to tell whether pathogen dynamics are still diverging from the original attractor due to a long-term perturbation, or have entered the basin of attraction of a new attractor. Now that several years have passed since major interventions have been lifted, many respiratory pathogens may have had sufficient time to begin returning to their post-intervention attractors—empirical comparisons between current cases and pre-pandemic cases are consistent with this hypothesis (Figure 1). With recent data, we can start to evaluate whether we see early signs of convergence to the former attractor or a new one.

Inferring pathogen resilience from real data

Based on these patterns, we now lay out our approach to estimating pathogen resilience from real data (Figure 3). We first tested this approach against simulations and applied it to real data. Specifically, we analyzed case time series of respiratory pathogens from four countries: Canada, Hong Kong, Korea, and the US.

So far, we have focused on simple examples that assume a constant transmission reduction during the pandemic. However, in practice, the impact of pandemic perturbations on pathogen transmission is likely more complex (Figure 3A), reflecting the introduction and relaxation of various intervention strategies. In some cases, strong perturbations likely caused local fadeouts, requiring immigration/importation from another location for epidemic rebound. Such complexities could lead to longer delays between the introduction of pandemic perturbations and pathogen rebound as well as temporal variation in outbreak sizes (Figure 3B); in this example, continued transmission reduction from interventions limits the size of the first outbreak in 2021 following the rebound, allowing for a larger outbreak in 2022 when interventions are further relaxed.

Previously, we relied on the dynamics of susceptible and infected hosts to compute the distance from the attractor (Figure 2), but information on susceptible hosts is rarely available in practice. In addition, uncertainties in case counts due to observation error, strain evolution, and multiannual cycles in the observed epidemic dynamics (e.g., adenovirus circulation patterns in Hong Kong and Korea) add challenges to defining pre-pandemic attractors, which limits our ability to measure the distance from the attractor. To address these challenges, we can reconstruct an em-

206 empirical attractor by utilizing Takens' theorem [17], which states that an attractor of a
207 nonlinear multidimensional system can be mapped onto a delayed embedding (Materials
208 and Methods). For example, we can use delayed logged values of pre-pandemic
209 cases $C(t)$ (Figure 3C) to reconstruct the attractor:

$$\langle \log(C(t) + 1), \log(C(t - \tau) + 1), \dots, \log(C(t - (M - 1)\tau) + 1) \rangle, \quad (1)$$

210 where the delay τ and embedding dimension M are determined based on autocor-
211 relations and false nearest neighbors, respectively [21, 22]. This allows us to define
212 the pre-pandemic attractor as a points on an M -dimensional space. We can then
213 apply the same delay and embedding dimensions to the entire time series to deter-
214 mine the position in multi-dimensional state space (Figure 3D), which allows us to
215 measure the nearest neighbor distance between the current state of the system and
216 the empirical pre-pandemic attractor (Figure 3E). Specifically, the nearest neighbor
217 distance is calculated by computing the distance between the current position on
218 the M -dimensional space and all points in the empirical attractor set and taking the
219 minimum value. In theory, we can now quantify how fast this distance decreases by
220 fitting a linear regression on a log scale, where the slope of the linear regression em-
221 pirically measures pathogen resilience, with a steeper slope corresponding to a higher
222 resilience estimate (Figure 3E). However, resulting estimates of pathogen resilience
223 can be sensitive to choices about embedding delays and dimensions. For example,
224 using longer delays and higher dimensions tends to smooth out temporal variations
225 in the distance from the attractor (Supplementary Figure S6).

226 Complex changes in the distance from the attractor suggest that estimating
227 pathogen resilience from linear regression will be particularly sensitive to our choice
228 of fitting windows for the regression (Figure 3E). Therefore, before we tried estimat-
229 ing resilience from real data, we explored an automated window selection criteria
230 for linear regression and tested it against randomized, stochastic simulations across
231 a range of realistic pandemic perturbation shapes. In doing so, we also explored
232 optimal choices for embedding dimensions and evaluated our choices of fitting win-
233 dows parameters and embedding dimensions by quantifying correlation coefficients
234 between the estimated resilience and the intrinsic resilience of a seasonally unforced
235 system (Materials and Methods). Overall, we found large variation in estimation
236 performances with correlation coefficients ranging from 0.21 to 0.61 (Supplementary
237 Figure S7). In almost all cases, the automated window selection approach outper-
238 formed a naive approach, which performs regression using all data from the the
239 timing of peak distance to current time (Supplementary Figure S7).

240 Based on the best-performing window selection criteria and embedding dimen-
241 sion, we applied this approach to pathogen surveillance data presented in Figure
242 1 (Materials and Methods). For each time series, we applied Takens' theorem in-
243 dependently to reconstruct the empirical attractor and obtained the corresponding
244 time series of distances from attractors (Supplementary Figure S8). Then, we used
245 the automated window selection criteria to fit a linear regression and estimated the
246 empirical resilience for each pathogen in each country (Supplementary Figure S8);

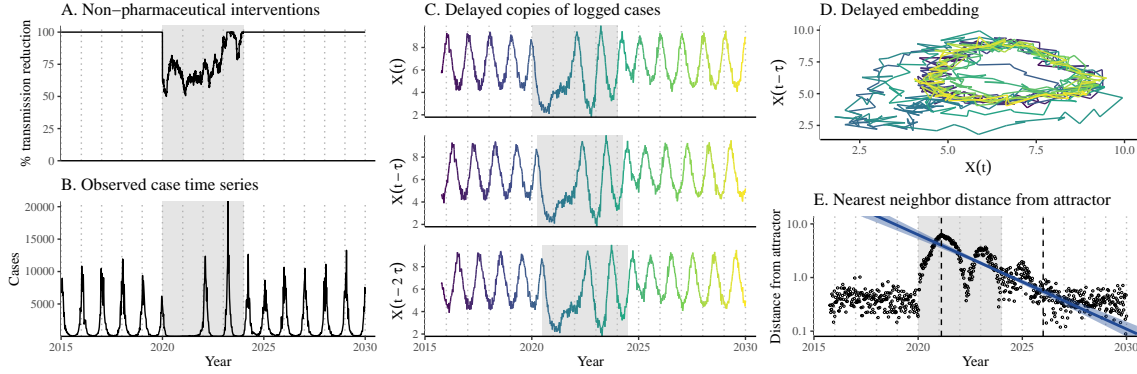


Figure 3: **A schematic diagram explaining the inference of pathogen resilience from synthetic data.** (A) A realistic example of simulated pandemic perturbations, represented by a relative reduction in transmission. (B) The impact of the synthetic pandemic perturbation on epidemic dynamics simulated using a SIRS model with demographic stochasticity. (C) Generating delayed copies of the logged time series allows us to obtain an embedding. (D) Two dimensional representation of an embedding. (E) Delayed embedding allows us to calculate the nearest neighbor distance from the empirical attractor, which is determined based on the pre-pandemic time series. Blue lines and dashed regions represent the linear regression fit and the associated 95% confidence interval. This distance time series can be used to infer pathogen resilience after choosing an appropriate window for linear regression. For illustration purposes, an arbitrary fitting window was chosen.

the window selection criteria gave poor regression windows in three cases (norovirus in Hong Kong and Korea and rhinovirus/enterovirus in the US), leading to unrealistically low resilience estimates, and so we used ad-hoc regression windows instead (Supplementary Figure S9; Materials and Methods).

For all pathogens we considered, resilience estimates fall between 0.4/year and 1.8/year (Figure 4A). We estimated the mean resilience of common respiratory pathogens to be 0.99/year (95% CI: 0.81/year–1.18/year). For reference, this is ≈ 7.5 times higher than the intrinsic resilience of pre-vaccination measles in England and Wales ($\approx 0.13/\text{year}$). Finally, resilience estimates for norovirus, a gastrointestinal pathogen, were comparable to those of common respiratory pathogens: 1.44/year (95% CI: 1.01/year–1.87/year) for Hong Kong and 1.07/year (95% CI: 0.86/year–1.29/year) for Korea. Based on a simple ANOVA test, we did not find significant differences in resilience estimates across countries ($p = 0.25$) or pathogens ($p = 0.67$).

Using resilience estimates, we predicted when each pathogen would hypothetically return to their pre-pandemic dynamics, assuming no long-term change in the attractor. Specifically, we extended our linear regression fits to distance-from-attractor time series and ask when the predicted regression line will cross a threshold value; since we relied on nearest neighbor distances, pre-pandemic distances are always greater than zero (Figure 3E), meaning that we can use the mean of pre-pandemic

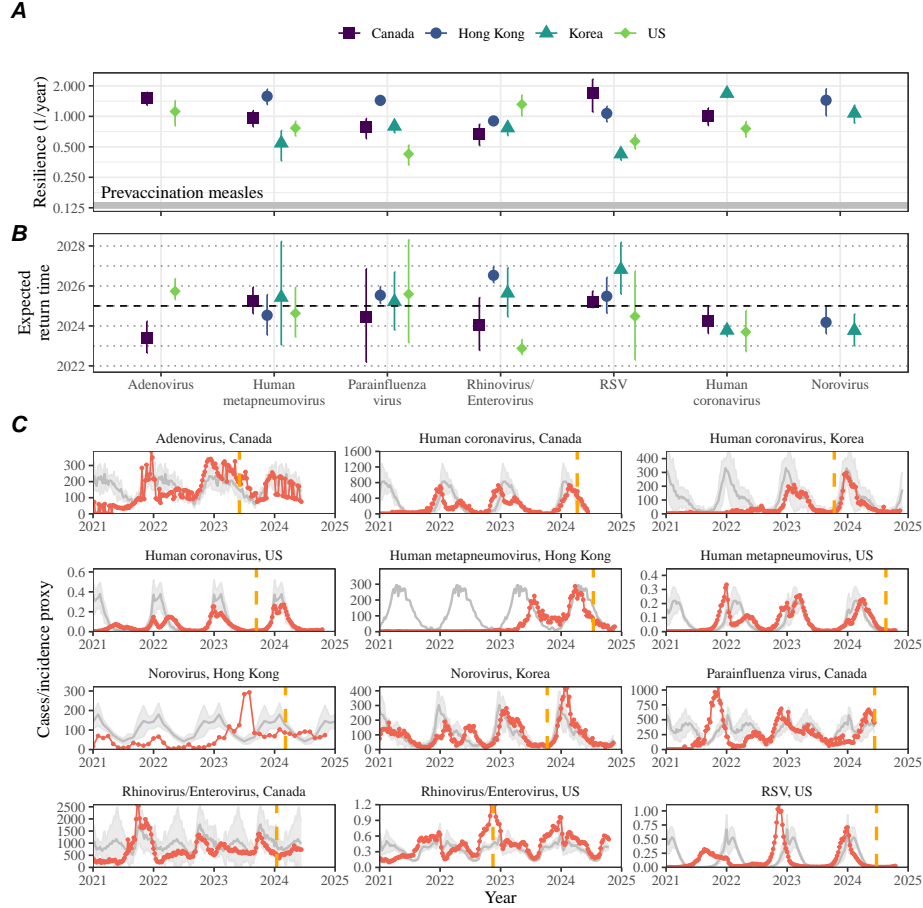


Figure 4: **Summary of resilience estimates and predictions for return time.** (A) Estimated pathogen resilience. The gray horizontal line represents the intrinsic resilience of pre-vaccination measles dynamics. (B) Predicted timing of when each pathogen will return to their pre-pandemic cycles. The dashed line in panel B indicates the end of 2024. Error bars represent 95% confidence intervals. (C) Observed dynamics for pathogen that are predicted to have returned before the end of 2024. Red points and lines represent data before 2020. Gray lines and shaded regions represent the mean seasonal patterns and corresponding 95% confidence intervals around the mean, previously shown in Figure 1. Orange vertical lines represent the predicted timing of return.

266 distances as our threshold.

267 We predicted that a return to pre-pandemic cycles has occurred or would be
 268 imminent for most pathogens (Figure 4B). In particular, we predicted that 12 out
 269 of 23 pathogen-country pairs should have already returned before the end of 2024.
 270 For almost all pathogens that were predicted to have returned already, the observed
 271 epidemic dynamics showed clear convergence towards their pre-pandemic seasonal

averages, confirming our predictions (Figure 4C). However, there were a few exceptions, including norovirus in Hong Kong and rhinovirus/enterovirus in the US, where the observed epidemic dynamics in 2024 exhibit clear deviation from their pre-pandemic seasonal averages (Figure 4C; Figure S9). These observations suggest a possibility that some common respiratory pathogens may have converged to different attractors or are still exhibiting non-equilibrium dynamics. In contrast, pathogens that were predicted to have not returned yet also showed clear differences from their pre-pandemic seasonal averages; as many of these pathogens are predicted to return in 2025–2026, we may be able to test these predictions in near future (Supplementary Figure S10). Our reconstructions of distance time series and estimates of pathogen resilience and expected return time were generally robust to choices of embedding dimensions (Supplementary Figure S11–12).

Susceptible host dynamics explain variation in pathogen resilience

So far, we have focused on quantifying pathogen resilience from the observed patterns of pathogen re-emergence following pandemic perturbations. But what factors determine the resilience of a host-pathogen system? To address this question, we used the SIRS model to explore how changes in susceptible host dynamics affect pathogen resilience. To do so, we varied the basic reproduction number \mathcal{R}_0 , which represents the average number of secondary infections caused by a newly infected individual in a fully susceptible population, and the duration of immunity and computed intrinsic resilience for each parameter.

We found that an increase in \mathcal{R}_0 and a decrease in the duration of immunity correspond to an increase in pathogen resilience (Figure 5A). Similarly, an increase in \mathcal{R}_0 and a decrease in the duration of immunity corresponds to a faster per-capita rate of susceptible replenishment, which is defined as the ratio between absolute rate at which new susceptibles enter the population and the equilibrium number of susceptible individuals in the population, S^* (Figure 5B). We note that a higher \mathcal{R}_0 drives a faster per-capita susceptible replenishment rate by decreasing the susceptible proportion at equilibrium, S^* . For a simple SIR model that assumes a life-long immunity, we can show analytically that pathogen resilience is proportional to the per-capita rate of susceptible replenishment (Materials and Methods). Overall, these observations suggest that a faster per-capita susceptible replenishment rate causes the system to be more resilient.

By taking the average values of empirical resilience for each pathogen, we were able to map each pathogen onto a set of parameters of the SIRS model that are consistent with corresponding resilience estimates (Figure 5A). Across all pathogens we considered, we estimated that the average duration of immunity is likely to be short (< 4 years) across a plausible range of \mathcal{R}_0 (< 6). We were also able to obtain a plausible range of susceptible replenishment rates for each pathogen (Figure 5B),

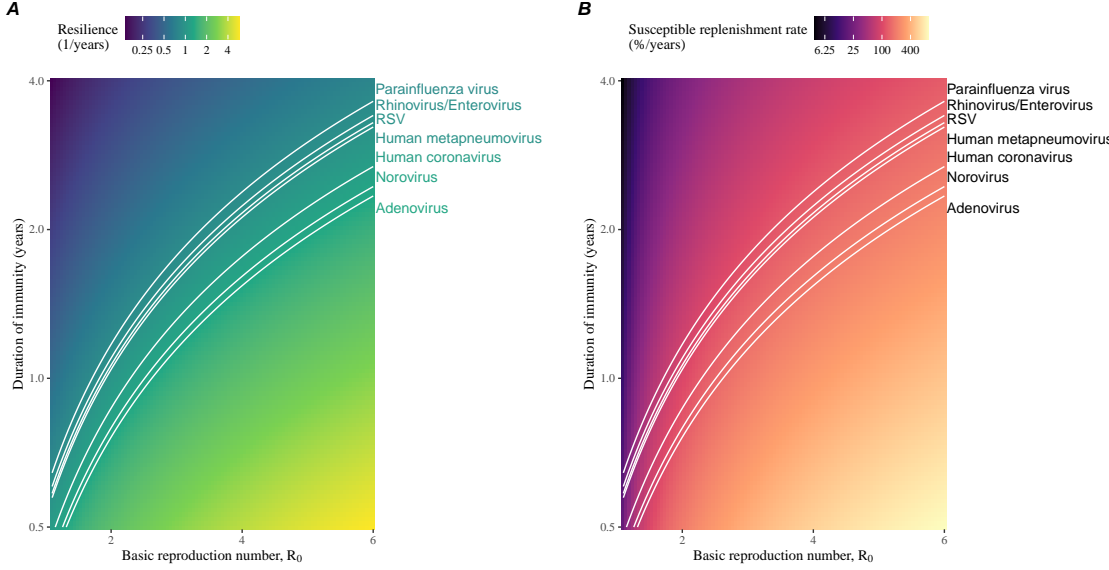


Figure 5: Linking pathogen resilience to epidemiological parameters and susceptible host dynamics. (A) Intrinsic resilience as a function of the basic reproduction number \mathcal{R}_0 and the duration of immunity. (B) Per-capita susceptible replenishment rate as a function of the basic reproduction number \mathcal{R}_0 and the duration of immunity. The standard SIRS model without seasonal forcing is used to compute intrinsic resilience and the per-capita susceptible replenishment rate. Lines correspond to a set of parameters that are consistent with mean resilience estimates for each pathogen, averaged across different countries.

312 but there was a large uncertainty in the estimates for susceptible replenishment rates
 313 due to a lack of one-to-one correspondence between susceptible replenishment rates
 314 and pathogen resilience.

315 **Pathogen resilience determines sensitivity to stochastic perturbations**

317 Even in the absence of major pandemic perturbations, host-pathogen systems are
 318 expected to experience continued perturbations of varying degrees from changes in
 319 epidemiological conditions, such as human behavior, climate, and viral evolution.
 320 These perturbations can also arise from demographic stochasticity, which is inher-
 321 ent to any ecological system. Here, we used a seasonally unforced SIRS model with
 322 constant birth and death rates to explore how resilience of a host-pathogen sys-
 323 tem determines the sensitivity to perturbations caused by demographic stochasticity
 324 (Materials and Methods).

325 We found that resilience of a host-pathogen system determines the amount of de-

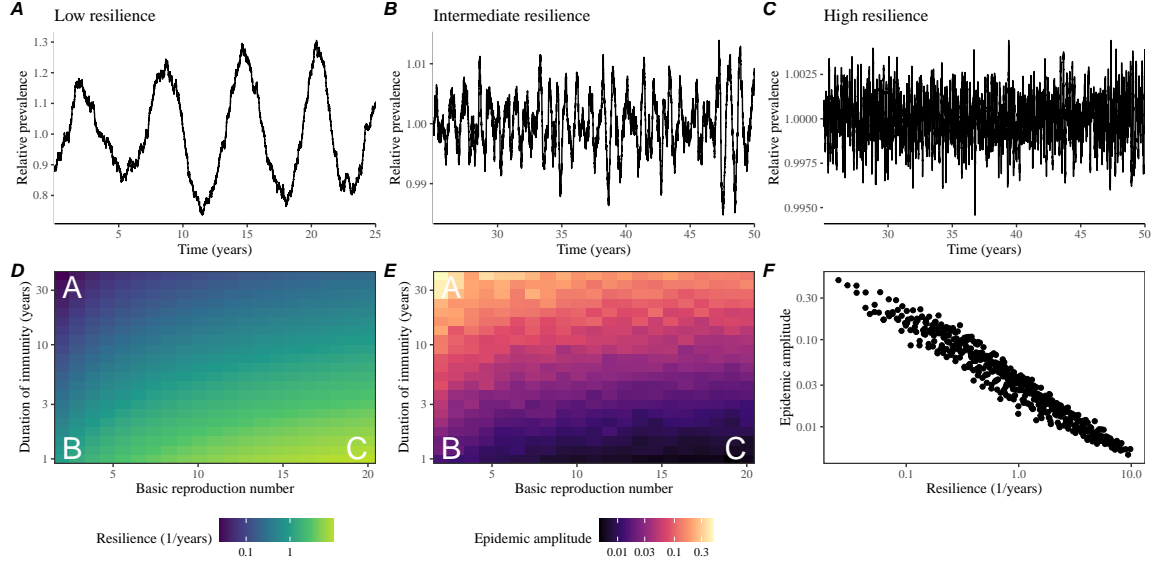


Figure 6: Linking resilience of a host-pathogen system to its sensitivity to stochastic perturbations. (A–C) Epidemic trajectories of a stochastic SIRS model across three different resilience values: low, intermediate, and high. The relative prevalence was calculated by dividing infection prevalence by its mean value. (D) Intrinsic resilience of a system as a function of the basic reproduction number \mathcal{R}_0 and the duration of immunity. (E) Epidemic amplitude as a function of the basic reproduction number \mathcal{R}_0 and the duration of immunity. The epidemic amplitude corresponds to $(\max I - \min I)/(2\bar{I})$, where \bar{I} represents the mean prevalence. Labels A–C in panels D and E correspond to scenarios shown in panels A–C. (F) The relationship between pathogen resilience and epidemic amplitude.

326 deviation from the deterministic trajectory caused by demographic stochasticity, with
 327 less resilient systems experiencing larger deviations (Figure 6). Notably, less resilient
 328 systems also exhibited slower epidemic cycles (Figure 6A–C). The periodicity of this
 329 epidemic cycle matched those predicted by the intrinsic periodicity of the system
 330 (Supplementary Figure S13) where the intrinsic resilience of the system is inversely
 331 proportional to its intrinsic periodicity (Supplementary Figure S14). However, we
 332 note that the interplay between seasonal transmission and intrinsic periodicity can
 333 also lead to complex cycles, as illustrated by a recent analysis of *Mycoplasma pneumoniae*
 334 dynamics [23].

335 We also note that the intrinsic resilience is not the sole determinant for how sen-
 336 sitive the system is to stochastic perturbations. For example, the population size
 337 and average duration of infection also affect the amount of deviation from the deter-
 338 ministic trajectory caused by demographic stochasticity, even though these quantities
 339 have little to no impact on the intrinsic resilience (Supplementary Figure S15). These
 340 conclusions were robust for the seasonally forced SIRS model (Supplementary Figure

³⁴¹ S16).

³⁴² Discussion

³⁴³ COVID-19 pandemic interventions caused major disruptions to circulation patterns
³⁴⁴ of both respiratory and non-respiratory pathogens, adding challenges to predicting
³⁴⁵ their future dynamics [1, 2, 3, 4]. However, these perturbations offer large-scale natural
³⁴⁶ experiments for understanding how different pathogens respond to perturbations.
³⁴⁷ In this study, we showed that pathogen re-emergence patterns following pandemic
³⁴⁸ perturbations can be characterized through the lens of ecological resilience and pre-
³⁴⁹ sented a new method for estimating pathogen resilience from time series data. We
³⁵⁰ showed that variation in pathogen resilience can be explained by the differences in
³⁵¹ susceptible host dynamics, where faster replenishment of the susceptible pool corre-
³⁵² sponds to a more resilient host-pathogen system. Finally, we showed that pathogen
³⁵³ resilience also determines the sensitivity to stochastic perturbations.

³⁵⁴ We analyzed case time series of common respiratory infections and norovirus
³⁵⁵ infections from Canada, Hong Kong, Korea, and the US to estimate their resilience.
³⁵⁶ Overall, we estimated the resilience of these pathogens to range from 0.4/year to
³⁵⁷ 1.8/year, which is 3–14 times more resilient than prevaccination measles. Consistent
³⁵⁸ with other epidemiological evidence [24, 25, 26, 27], these resilience estimates indicate
³⁵⁹ that common respiratory pathogens and norovirus likely exhibit faster susceptible
³⁶⁰ replenishment and are therefore more persistent, indicating potential challenges in
³⁶¹ controlling these pathogens.

³⁶² Based on our resilience estimates, we made phenomenological predictions about
³⁶³ when each pathogen will return to their endemic cycles. For the most part, we
³⁶⁴ accurately predicted which pathogens should have already returned before the end
³⁶⁵ of 2024. However, there were two main exceptions (i.e., norovirus in Hong Kong
³⁶⁶ and rhinovirus/enterovirus in the US), suggesting that these pathogens may be con-
³⁶⁷ verging to new endemic cycles or experiencing long-term transient behavior. These
³⁶⁸ changes may reflect changes in surveillance or actual shift in the dynamics, caused
³⁶⁹ by permanent changes in behavior or population-level immunity. While it may seem
³⁷⁰ unlikely that permanent changes in behavior would only affect a few pathogens and
³⁷¹ not others, we cannot rule out this possibility given differences in the observed mean
³⁷² age of infections and therefore the differences in age groups that primarily drive
³⁷³ transmission [28, 29]. Differences in the mode of transmission between respiratory
³⁷⁴ vs gastrointestinal pathogens may also contribute to the differences in responses to
³⁷⁵ pandemic perturbations.

³⁷⁶ For almost half of the pathogens we considered, we predicted that their return
³⁷⁷ to original epidemic patterns is imminent. We will need a few more years of data
³⁷⁸ to test whether these pathogens will eventually return to their original dynamics or
³⁷⁹ eventually converge to a different attractor. We also cannot rule out the possibility
³⁸⁰ that some pathogens may exhibit long-term transient behaviors following pandemic

381 perturbations. Overall, these observations echo earlier studies that highlighted the
382 long-lasting impact of pandemic perturbations [8, 30, 31, 4, 23].

383 We showed that susceptible host dynamics shape pathogen resilience, where faster
384 replenishment of the susceptible population causes the pathogen to be more resilient.
385 For simplicity, we focused on waning immunity and birth as the main drivers of the
386 susceptible host dynamics but other mechanisms can also contribute to the replen-
387 ishment of the susceptible population. In particular, pathogen evolution, especially
388 the emergence of antigenically novel strains, can cause effective waning of immunity
389 in the population; therefore, we hypothesize that the rate of antigenic evolution is
390 likely a key feature of pathogen resilience. Future studies should explore the relation-
391 ship between the rate of evolution and resilience for antigenically evolving pathogens.
392 This result also highlights the importance of detailed measurements of changes in the
393 susceptible population through immune assays for understanding pathogen dynamics
394 [32].

395 Quantifying pathogen resilience also offers novel approaches to validating population-
396 level epidemiological models. So far, most model validation in infectious disease ecol-
397 ogy is based on the ability of a model to reproduce the observed epidemic dynamics
398 and to predict future dynamics [33, 34, 26, 35, 36]. However, many models can
399 perform similarly under these criteria. For example, two major RSV models have
400 been proposed to explain biennial epidemic patterns: (1) a stage- and age-structured
401 model that allows disease severity to vary with number of past infections and age of
402 infection [26] and (2) a pathogen-interaction model that accounts for cross immunity
403 between RSV and human metapneumovirus [34]. Since both models can accurately
404 reproduce the observed epidemic patterns, standard criteria for model validation
405 do not allow us to distinguish between these two models from population-level data
406 alone. Instead, it would be possible to measure the empirical resilience of each model
407 by simulating various perturbations and comparing the simulations to estimates of
408 empirical resilience from data, using pandemic perturbations as a reference.

409 There are several limitations to our work. First, we did not extensively explore
410 other approaches to reconstructing the attractor. Recent studies showed that more
411 sophisticated approaches, such as using non-uniform embedding, can provide more
412 robust reconstruction for noisy data [22]. In the context of causal inference, choices
413 about embedding can have major impact on the resulting inference [37]. Our re-
414 silience estimates are likely overly confident given a lack of uncertainties in attractor
415 reconstruction as well as the simplicity of our statistical framework. Nonetheless,
416 as illustrated in our sensitivity analyses, inferences about pathogen resilience in our
417 SIRS model appear to be robust to decisions about embedding lags and dimensions—
418 this is because tracking the rate at which the system approaches the attractor is likely
419 a much simpler problem than making inferences about causal directionality. Short
420 pre-pandemic time series also limit our ability to accurately reconstruct the attrac-
421 tor and contribute to the crudeness of our resilience estimates; although this is less
422 likely a problem for respiratory pathogens that are strongly annual, our attractor
423 reconstruction may be inaccurate for those exhibiting multi-annual cycles, such as

424 adenovirus in Hong Kong and Korea. Our framework also does not allow us to dis-
425tinguish whether a system has settled to a new attractor or is experiencing long-term
426 transient behavior. Uncertainties in pathogen dynamics due to changes in testing
427 patterns further contribute to the crudeness of our resilience estimates.

428 While attractor reconstruction allows us to make model-free inferences of pathogen
429 resilience, it does not allow us to tease apart how different mechanisms contribute
430 to the resilience a host-pathogen system. Using the simple SIRS model, we illus-
431 trated that susceptible host dynamics are key determinants of pathogen resilience,
432 but we also found that there isn't a one-to-one correspondence between per capita
433 replenishment rate of the susceptible population and pathogen resilience estimates.
434 Future studies should explore using mechanistic models to explain heterogeneity in
435 resilience estimates across different pathogens.

436 Finally, our simulation-based analyses primarily focused on single-strain systems,
437 but real-world pathogens can interact with other pathogens, which can result in com-
438 plex dynamics [38, 39]. To address this limitation, we considered a simple model of
439 two competing strains (via cross immunity) and showed that the resilience of a cou-
440 pled system can be measured by studying the dynamics of either strain. However, this
441 conclusion likely depends on the strength and mechanism of strain interactions. For
442 example, ecological interference between two unrelated pathogens [38] will likely gen-
443 erate weaker coupling than cross-immunity between related pathogens; in the former
444 case, we do not necessarily expect two unrelated pathogens to have same resilience
445 despite their ecological interference. Some pathogen strains can also exhibit positive
446 interactions where infection by one strain can lead to an increased transmission of
447 another competing strain. For example, previous studies showed that an increased
448 dengue transmission through antibody-dependent enhancement can permit coexis-
449 tence and persistence of competing strains [40]; since pathogen transmissibility is a
450 major determinant of pathogen resilience, we tentatively hypothesize that positive
451 interactions such as antibody-dependent enhancement may increase the resilience of
452 a system. Future studies should explore how different mechanisms of pathogen inter-
453 actions contribute to the resilience of each competing pathogen as well as the entire
454 system. Despite these limitations, our study illustrates that quantifying pathogen
455 resilience can provide novel insights into pathogen dynamics. Furthermore, our qual-
456 itative prediction that common respiratory pathogens are more resilient than pre-
457 vaccination measles is also likely to be robust, given how rapidly many respiratory
458 pathogens returned to their original cycles following pandemic perturbations.

459 Predicting the impact of anthropogenic changes on infectious disease dynamics
460 is a fundamental aim of infectious disease research in a rapidly changing world. Our
461 study illustrates that how a host-pathogen system responds to both small and large
462 perturbations is largely predictable through the lens of ecological resilience. In par-
463 ticular, quantifying the resilience of a host-pathogen system offers a unique insight
464 into questions about endemic pathogens' responses to pandemic perturbations, in-
465 cluding whether some pathogens will exhibit long-lasting impact from the pandemic
466 perturbation or not. More broadly, a detailed understanding of the determinants of

467 pathogen resilience can provide deeper understanding of pathogen persistence.

468 Materials and Methods

469 Data

470 We gathered time series on respiratory infections from Canada, Hong Kong, Korea,
471 and United States (US). As a reference, we also included time series data on norovirus
472 infections when available. In contrast to respiratory pathogens, we hypothesized
473 gastrointestinal viruses, such as norovirus, to be differently affected by pandemic
474 perturbations.

475 Weekly time series of respiratory infection cases in Canada came from a publicly
476 available website by the Respiratory Virus Detection Surveillance System, which
477 collects data from select laboratories across Canada [41]. Weekly time series of
478 respiratory infection cases in Hong Kong came from a publicly available website
479 by the Centre for Health Protection, Department of Health [42, 43]. Weekly time
480 series of acute respiratory infection cases in Korea came from a publicly available
481 website by the Korea Disease Control and Prevention Agency [44]. Finally, weekly
482 time series of respiratory infection cases in the US were obtained from the National
483 Respiratory and Enteric Virus Surveillance System (NREVSS). Readers can request
484 the data from NREVSS at nrevss@cdc.gov. Time series on number of tests were also
485 available in Canada, Hong Kong, and the US, but not in Korea.

486 Data processing

487 For all time series, we rounded every year to 52 weeks by taking the average number
488 of cases and tests between the 52nd and 53rd week. We also rescaled all time series to
489 account for changes in testing patterns, which were then used for the actual analysis.

490 For Canada, an increase in testing was observed from 2013 to 2024 (Supplementary
491 Figure S17). To account for this increase, we calculated a 2 year moving average
492 for the number of tests for each pathogen, which we used as a proxy for testing effort.
493 Then, we divided the smoothed testing patterns by the smoothed value at the final
494 week such that the testing effort has a maximum of 1. We then divided weekly cases
495 by the testing effort to obtain a scaled case time series. A similar approach was used
496 earlier for an analysis of RSV time series in the US to account for changes in testing
497 patterns [26].

498 For Hong Kong, we applied the same scaling procedure to the time series as we
499 did for Canada. In this case, we only adjusted for testing efforts up to the end of 2019
500 because there was a major reduction in testing for common respiratory pathogens
501 between 2020 and 2023 (Supplementary Figure S18).

502 For Korea, while we did not have information on testing, the reported number
503 of respiratory infections consistently increased from 2013 to the end of 2019, which
504 we interpreted as changes in testing patterns (Supplementary Figure S19). Since

505 we did not have testing numbers, we used the weekly sum of all acute respiratory
506 viral infection cases as a proxy for testing, which were further smoothed with moving
507 average and scaled to have a maximum of 1. For Korea, we also only adjusted for
508 testing efforts up to the end of 2019.

509 In the US, there has been a large increase in testing for some respiratory pathogens,
510 especially RSV, which could not be corrected by simple scaling (Supplementary Fig-
511 ure S20). Instead, we derived an incidence proxy by multiplying the test positivity
512 with influenza-like illness positivity, which was taken from <https://gis.cdc.gov/grasp/fluvie...>. This method of estimating an inci-
513 dence proxy has been recently applied in the analysis of seasonal coronaviruses [7]
514 and *Mycoplasma pneumoniae* infections [4]. Detailed assumptions and justifications
515 are provided in [45].

517 Data summary

518 To make qualitative comparisons between pre- and post-perturbation dynamics of
519 respiratory pathogen circulation patterns, we calculated the mean seasonal patterns
520 using time series of either rescaled cases or incidence proxy estimates before 2020. We
521 did so by taking the mean value in each week across all years before 2020. Confidence
522 intervals around the means were calculated using a simple t test.

523 Estimating pathogen resilience

524 In order to measure pathogen resilience from surveillance data, we first reconstructed
525 the empirical pre-pandemic attractor of the system using Takens' embedding theorem
526 [17]. Specifically, for a given pathogen, we took the pre-pandemic (before 2020) case
527 time series $C(t)$ and reconstructed the attractor using delayed embedding with a
528 uniform delay of τ and dimension M :

$$X_{\tau,m}(t) = \langle \log(C(t) + 1), \log(C(t - \tau) + 1), \dots, \log(C(t - (M - 1)\tau) + 1) \rangle. \quad (2)$$

529 Here, the delay τ was determined by calculating the autocorrelation of the logged
530 pre-pandemic time series and asking when the autocorrelation crosses 0 for the first
531 time [22]; a typical delay for an annual outbreak is around 13 weeks.

532 Then, for a given delay τ , we determined the embedding dimension M using the
533 false nearest neighbors approach [21, 22]. To do so, we started with an embedding
534 dimension e and constructed a set of points $A_{\tau,e} = \{X_{\tau,e}(t) | t < 2020\}$. Then, for
535 each point $X_{\tau,e}(t)$, we determined the nearest neighbor from the set $A_{\tau,e}$, which we
536 denote $X_{\tau,e}(t_{nn})$ for $t \neq t_{nn}$. Then, if the distance between these two points in the
537 $e+1$ dimension, $D_{\tau,e+1}(t) = \|X_{\tau,e+1}(t_{nn}) - X_{\tau,e+1}(t)\|_2$, is larger than their distance in
538 the e dimension, $D_{\tau,e}(t) = \|X_{\tau,e}(t_{nn}) - X_{\tau,e}(t)\|_2$, these two points are deemed to be
539 false nearest neighbors; specifically, we used a threshold R for the ratio between two
540 distances $D_{\tau,e+1}(t)/D_{\tau,e}(t)$ to determine false nearest neighbors. The first embed-
541 ding dimension e that does not have any false nearest neighbors corresponds to the

embedding dimension M for a given pathogen-country pair. For the main analysis, we used $R = 10$, which was chosen from a sensitivity analysis against simulated data (Supplementary Text). Once we determined the embedding lag τ and dimension M , we apply the embedding to the entire time series and calculate the nearest neighbor distance against the attractor $A_{\tau,M}$ to obtain a time series of distance from the attractor $D_{\tau,M}(t)$.

From a time series of distances from the attractor, we estimated pathogen resilience by fitting a linear regression to an appropriate window. To automatically select fitting windows, we began by smoothing the distance time series using locally estimated scatterplot smoothing (LOESS) to obtain $\hat{D}_{\tau,M}(t)$, where the smoothing is performed on a log scale and exponentiated afterwards. This smoothing allowed us to find appropriate threshold values for selecting fitting windows that are insensitive to errors in our estimates of distance from the attractor. Then, we determined threshold values (T_{start} and T_{end}) for the smoothed distances and choose the fitting window based on when $\hat{D}_{\tau,M}(t)$ crosses these threshold values for the first time. These thresholds were determined by first calculating the maximum distance,

$$\max \hat{D} = \max \hat{D}_{\tau,M}(t), \quad (3)$$

and the mean pre-pandemic distance,

$$\hat{D}_{\text{mean}} = \frac{1}{N_{t < 2020}} \sum_{t < 2020} \hat{D}_{\tau,M}(t), \quad (4)$$

as a reference, and then dividing their ratios into K equal bins,

$$T_{\text{start}} = \hat{D}_{\text{mean}} \times \left(\frac{\max \hat{D}}{\hat{D}_{\text{mean}}} \right)^{(K-a)/K}, \quad (5)$$

$$T_{\text{end}} = \hat{D}_{\text{mean}} \times \left(\frac{\max \hat{D}}{\hat{D}_{\text{mean}}} \right)^{a/K}, \quad (6)$$

where a represents the truncation threshold. This allows us to discard the initial period during which the distance increases (from the introduction of intervention measures) and the final period during which the distance plateaus (as the system reaches an attractor). The fitting window is determined based on when the smoothed distance $\hat{D}_{\tau,M}(t)$ crosses these threshold values for the first time; then, we fit a linear regression to logged (unsmoothed) distances $\log D_{\tau,M}(t)$ using that window. Alongside the threshold R for the false nearest neighbors approach, we tested optimal choices for K and a values using simulations (Supplementary Text). We used $K = 19$ and $a = 2$ throughout the paper based on the simulation results.

Mathematical modeling

Throughout the paper, we use a series of mathematical models to illustrate the concept of pathogen resilience and to understand the determinants of pathogen re-

572 silience. In general, the intrinsic resilience of a given system is given by the largest
 573 real part of the eigenvalues of the linearized system at endemic equilibrium. Here, we
 574 focus on the SIRS model with demography (birth and death) and present the details
 575 of other models in Supplementary Text. The SIRS (Susceptible-Infected-Recovered-
 576 Susceptible) model is the simplest model that allows for waning of immunity, where
 577 recovered (immune) individuals are assumed to become fully susceptible after an
 578 average of $1/\delta$ time period. The dynamics of the SIRS model is described by the
 579 following set of differential equations:

$$\frac{dS}{dt} = \mu - \beta(t)SI - \mu S + \delta R \quad (7)$$

$$\frac{dI}{dt} = \beta(t)SI - (\gamma + \mu)I \quad (8)$$

$$\frac{dR}{dt} = \gamma I - (\delta + \mu)R \quad (9)$$

580 where μ represents the birth and death rates, $\beta(t)$ represents the time-varying trans-
 581 mission rate, and γ represents the recovery rate. The basic reproduction number
 582 $\mathcal{R}_0(t) = \beta(t)/(\gamma + \mu)$ is defined as the average number of secondary infections that
 583 a single infected individual would cause in a fully susceptible population at time t
 584 and measures the intrinsic transmissibility of a pathogen.

585 When we introduced the idea of pathogen resilience (Figure 2), we imposed sinu-
 586 soidal changes to the transmission rate to account for seasonal transmission,

$$\beta(t) = b_1(1 + \theta \cos(2\pi(t - \phi)))\alpha(t), \quad (10)$$

587 where b_1 represents the baseline transmission rate, θ represents the seasonal ampli-
 588 tude, and ϕ represents the seasonal offset term. Here, we also introduced an extra
 589 multiplicative term $\alpha(t)$ to account for the impact of pandemic perturbations, where
 590 $\alpha(t) < 1$ indicates transmission reduction. Figure 2A and 2B were generated assum-
 591 ing $b_1 = 3 \times (365/7 + 1/50)/\text{years}$, $\theta = 0.2$, $\phi = 0$, $\mu = 1/50/\text{years}$, $\gamma = 365/7/\text{years}$,
 592 and $\delta = 1/2/\text{years}$. Specifically, $b_1 = 3 \times (365/7 + 1/50)/\text{years}$ implies $\mathcal{R}_0 = 3$, where
 593 $(365/7 + 1/50)/\text{years}$ represent the rate of recovery. In Figure 2A, we imposed a 50%
 594 transmission reduction for 6 months from 2020:

$$\alpha(t) = \begin{cases} 0.5 & 2020 \leq t < 2020.5 \\ 1 & \text{otherwise} \end{cases} \quad (11)$$

595 In Figure 2B, we imposed a 50% transmission reduction for 6 months from 2020 and
 596 a permanent 10% reduction onward:

$$\alpha(t) = \begin{cases} 1 & t < 2020 \\ 0.5 & 2020 \leq t < 2020.5 \\ 0.9 & 2020.5 \leq t \end{cases} \quad (12)$$

597 In both scenarios, we simulated the SIRS model from the same initial conditions
 598 ($S(0) = 1/\mathcal{R}_0$, $I(0) = 1 \times 10^{-6}$, and $R(0) = 1 - S(0) - I(0)$) from 1900 until 2030.
 599 Throughout the paper, all deterministic models were solved using the `lsoda` solver
 600 from the `deSolve` package [46] in R [47].

601 To measure the empirical resilience of the SIRS model (Figure 2C and 2F), we
 602 computed the normalized distance between post-intervention susceptible and logged
 603 infected proportions and their corresponding unperturbed values at the same time:

$$\sqrt{\left(\frac{S(t) - S_{\text{unperturbed}}(t)}{\sigma_S}\right)^2 + \left(\frac{\log I(t) - \log I_{\text{unperturbed}}(t)}{\sigma_{\log I}}\right)^2}, \quad (13)$$

604 where σ_S and $\sigma_{\log I}$ represent the standard deviation in the unperturbed susceptible
 605 and logged infected proportions. The unperturbed values were obtained by simulating
 606 the same SIRS model without pandemic perturbations ($\alpha = 1$). We normalized
 607 the differences in susceptible and logged infected proportions to allow both quantities
 608 to equally contribute to the changes in distance from the attractor. We used logged
 609 prevalence, instead of absolute prevalence, in order to capture epidemic dynamics
 610 in deep troughs during the intervention period. In Supplementary Materials, we
 611 also compared how the degree of seasonal transmission affects empirical resilience
 612 by varying θ from 0 to 0.4; when we assumed no seasonality ($\theta = 0$), we did not
 613 normalize the distance because the standard deviation of pre-intervention dynamics
 614 are zero.

615 We used the SIRS model to understand how underlying epidemiological parameters
 616 affect pathogen resilience and determine the relationship to underlying susceptible host dynamics. For the simple SIRS model without seasonal transmission
 618 ($\theta = 0$), the intrinsic resilience equals

$$-\frac{\text{Re}(\lambda)}{2} = \frac{\delta + \beta I^* + \mu}{2}. \quad (14)$$

619 Here, I^* represents the prevalence at endemic equilibrium:

$$I^* = \frac{(\delta + \mu)(\beta - (\gamma + \mu))}{\beta(\delta + \gamma + \mu)}. \quad (15)$$

620 The susceptible replenishment rate is given by

$$S_{\text{replenish}} = \frac{\mu + \delta R}{S^*}, \quad (16)$$

621 where $S^* = 1/\mathcal{R}_0$ represents the equilibrium proportion of susceptible individuals.
 622 We varied the basic reproduction number \mathcal{R}_0 between 1.1 to 6 and the average
 623 duration of immunity $1/\delta$ between 2 to 4 years, and computed these two quantities.
 624 In doing so, we fixed all other parameters: $\mu = 1/80/\text{years}$ and $\gamma = 365/7/\text{years}$.
 625 When infection provides a life-long immunity ($\delta = 0$), the intrinsic resilience is
 626 inversely proportional to the susceptible replenishment rate:

$$-\frac{\text{Re}(\lambda)}{2} = \frac{\mu}{2S^*} = \frac{S_{\text{replenish}}}{2}. \quad (17)$$

627 Finally, we used a seasonally unforced stochastic SIRS model without demog-
628 raphy to understand how pathogen resilience affects sensitivity of the system to
629 demographic stochasticity (see Supplementary Text for the details of the stochas-
630 tic SIRS model). By varying the basic reproduction number \mathcal{R}_0 between 2 to 20
631 and the average duration of immunity $1/\delta$ between 1 to 40 years, we ran the SIRS
632 model for 100 years and computed the epidemic amplitude, which we defined as
633 $(\max I - \min I)/(2\bar{I})$. Each simulation began from the equilibrium, and we trun-
634 cated the initial 25 years before computing the epidemic amplitude. In doing so,
635 we assumed $\gamma = 365/7/\text{years}$ and fixed the population size to 1 billion to prevent
636 any fadeouts. We also considered a seasonally forced stochastic SIRS model without
637 demography, assuming an amplitude of seasonal forcing of 0.04; in this case, we com-
638 puted the relative epidemic amplitude by comparing the deterministic and stochastic
639 trajectories (Supplementary Materials).

640 Acknowledgement

641 We thank Centers for Disease Control and Prevention, National Respiratory and
642 Enteric Virus Surveillance System (NREVSS) for providing time series data for res-
643 piratory infection cases in the US.

644 Data availability

645 All data and code are stored in a publicly available GitHub repository (<https://github.com/cobeylab/return-time>).

647 Funding

648 S.W.P. is a Peter and Carmen Lucia Buck Foundation Awardee of the Life Sciences
649 Research Foundation. B.F.N. acknowledges financial support from the Carlsberg
650 Foundation (grant no. CF23-0173). B.T.G is supported by Princeton Catalysis Ini-
651 tiative and Princeton Precision Health. S.C. is supported by Federal funds from the
652 National Institute of Allergy and Infectious Diseases, National Institutes of Health,
653 Department of Health and Human Services under CEIRR contract 75N93021C00015.
654 The content is solely the responsibility of the authors and does not necessarily repre-
655 sent the official views of the NIAID or the National Institutes of Health. This project
656 has been funded in whole or in part with Federal funds from the National Cancer In-
657 stitute, National Institutes of Health, under Prime Contract No. 75N91019D00024,
658 Task Order No. 75N91023F00016 (B.F.N., E.H., and B.T.G). The content of this
659 publication does not necessarily reflect the views or policies of the Department of
660 Health and Human Services, nor does mention of trade names, commercial products
661 or organizations imply endorsement by the U.S. Government.

662 **Supplementary Text**

663 **Resilience of a stage-structured system.**

664 In Figure 2G–I, we used a more realistic, stage-structured model to illustrate how
 665 transient phenomena can cause the system to slow down. Specifically, we used the
 666 stage-structured RSV model proposed by [26], which assumes that subsequent rein-
 667 fections cause an individual to become less susceptible and transmissible than previ-
 668 ous infections. In contrast to a standard SIRS model, this model does not include a
 669 recovered compartment, which allow for temporary protection against new infections,
 670 and assumes that recovered individuals are immediately susceptible to new infections.
 671 The model dynamics can be described as follows:

$$\frac{dM}{dt} = \mu - (\omega + \mu)M \quad (S1)$$

$$\frac{dS_0}{dt} = \omega M - (\lambda(t) + \mu)S_0 \quad (S2)$$

$$\frac{dI_1}{dt} = \lambda(t)S_0 - (\gamma_1 + \mu)I_1 \quad (S3)$$

$$\frac{dS_1}{dt} = \gamma_1 I_1 - (\sigma_1 \lambda(t) + \mu)S_1 \quad (S4)$$

$$\frac{dI_2}{dt} = \sigma_1 \lambda(t)S_1 - (\gamma_2 + \mu)I_2 \quad (S5)$$

$$\frac{dS_2}{dt} = \gamma_2 I_2 - (\sigma_2 \lambda(t) + \mu)S_2 \quad (S6)$$

$$\frac{dI_3}{dt} = \sigma_2 \lambda(t)S_2 - (\gamma_3 + \mu)I_3 \quad (S7)$$

$$\frac{dS_3}{dt} = \gamma_3 I_3 - (\sigma_3 \lambda(t) + \mu)S_3 + \gamma_4 I_4 \quad (S8)$$

$$\frac{dI_4}{dt} = \sigma_3 \lambda(t)S_3 - (\gamma_4 + \mu)I_4 \quad (S9)$$

672 where M represents the proportion of individuals who are maternally immune; S_i
 673 represents the proportion of individuals who are susceptible after i prior infections; I_i
 674 represents the proportion of individuals who are currently (re)-infected with their i -th
 675 infection; μ represents the birth and death rates; $1/\omega$ represents the mean duration
 676 of maternal immunity; $1/\gamma_i$ represents the mean duration of infection; $\lambda(t)$ represents
 677 the force of infection; and σ_i represents the reduction in susceptibility for the i -th
 678 reinfection. The force of infection is modeled using a sinusoidal function:

$$\beta(t) = b_1(1 + \theta \cos(2\pi(t - \phi)))\alpha(t) \quad (S10)$$

$$\lambda(t) = \beta(I_1 + \rho_1 I_2 + \rho_2(I_3 + I_4)), \quad (S11)$$

679 where b_1 represents the baseline transmission rate; θ represents the seasonal ampli-
 680 tude; ϕ represents the seasonal offset term; $\alpha(t)$ represents the intervention effect;

and ρ_i represents the impact of immunity on transmission reduction. We used the following parameters to simulate the impact of interventions on epidemic dynamics [26]: $b_1 = 9 \times (365/10 + 1/80)/\text{years}$, $\theta = 0.2$, $\phi = -0.1$, $\omega = 365/112/\text{years}$, $\gamma_1 = 365/10/\text{years}$, $\gamma_2 = 365/7/\text{years}$, $\gamma_3 = 365/5/\text{years}$, $\sigma_1 = 0.76$, $\sigma_2 = 0.6$, $\sigma_3 = 0.4$, $\rho_1 = 0.75$, $\rho_2 = 0.51$, and $\mu = 1/80/\text{years}$. We assumed a 50% transmission reduction for 6 months from 2020:

$$\alpha(t) = \begin{cases} 0.5 & 2020 \leq t < 2020.5 \\ 1 & \text{otherwise} \end{cases} \quad (\text{S12})$$

The model was simulated from 1900 to 2030 using the following initial conditions: $M = 0$, $S_0 = 1/\mathcal{R}_0 - I_1$, $I_1 = 1 \times 10^{-6}$, $S_1 = 1 - 1/\mathcal{R}_0$, $I_2 = 0$, $S_2 = 0$, $I_3 = 0$, $S_3 = 0$, and $I_4 = 0$. For the phase plane analysis (Figure 2H) and distance analysis (Figure 2I), we relied on the average susceptibility,

$$\bar{S} = S_0 + \sigma_1 S_1 + \sigma_2 S_2 + \sigma_3 S_3, \quad (\text{S13})$$

and total prevalence,

$$I_{\text{total}} = I_1 + I_2 + I_3 + I_4. \quad (\text{S14})$$

These quantities were used to compute the normalized distance from the attractor, as described in the main text.

We note that this system, without seasonally forced transmission rates, has 9 eigenvalues: -73.01, -53.11, -38.90, -3.27, $-0.82+2.57i$, $-0.82-2.57i$, -1.61, -1.18, and -0.01 (in the unit of 1/years). While the eigenvalue -0.01 has the largest real part, the magnitude is too close to 0 for the impact of this eigenvalue to be reflected in our resilience estimates. Instead, we chose real parts of the eigenvalues $-0.82 \pm 2.57i$ as our intrinsic resilience for this system and plotted them in Figure 2I; as we can see in this figure, this value captures the return rate of the system to the attractor.

Resilience of a multistrain system.

We used a simple two-strain model to show that a multistrain host-pathogen system that is coupled through cross immunity can be described by a single resilience value. The model dynamics can be described as follows [34]:

$$\frac{dS}{dt} = \mu - \mu S - (\lambda_1 + \lambda_2)S + \delta_1 R_1 + \delta_2 R_2 \quad (\text{S15})$$

$$\frac{dI_1}{dt} = \lambda_1 S - (\gamma_1 + \mu)I_1 \quad (\text{S16})$$

$$\frac{dI_2}{dt} = \lambda_2 S - (\gamma_2 + \mu)I_2 \quad (\text{S17})$$

$$\frac{dR_1}{dt} = \gamma_1 I_1 - \lambda_2 \epsilon_{21} R_1 - \delta_1 R_1 + \delta_2 R - \mu R_1 \quad (\text{S18})$$

$$\frac{dR_2}{dt} = \gamma_2 I_2 - \lambda_1 \epsilon_{12} R_2 - \delta_2 R_2 + \delta_1 R - \mu R_2 \quad (\text{S19})$$

$$\frac{dJ_1}{dt} = \lambda_1 \epsilon_{12} R_2 - (\gamma_1 + \mu) J_1 \quad (S20)$$

$$\frac{dJ_2}{dt} = \lambda_2 \epsilon_{21} R_1 - (\gamma_2 + \mu) J_2 \quad (S21)$$

$$\frac{dR}{dt} = \gamma_1 J_1 + \gamma_2 J_2 - \delta_1 R - \delta_2 R - \mu R \quad (S22)$$

where S represents the proportion of individuals who are fully susceptible to infections by both strains; I_1 represents the proportion of individuals who are infected with strain 1 without prior immunity; I_2 represents the proportion of individuals who are infected with strain 2 without prior immunity; R_1 represents the proportion of individuals who are fully immune against strain 1 and partially susceptible to reinfection by strain 2; R_2 represents the proportion of individuals who are fully immune against strain 2 and partially susceptible to reinfection by strain 1; J_1 represents the proportion of individuals who are infected with strain 1 with prior immunity against strain 2; J_2 represents the proportion of individuals who are infected with strain 2 with prior immunity against strain 1; R represents the proportion of individuals who are immune to infections from both strains; μ represents the birth/death rate; λ_1 and λ_2 represent the force of infection from strains 1 and 2, respectively; δ_1 and δ_2 represent the waning immunity rate; γ_1 and γ_2 represent the recovery rate; ϵ_{21} and ϵ_{12} represent the susceptibility to reinfection with strains 2 and 1, respectively, given prior immunity from infection with strains 1 and 2, respectively. The force of infection is modeled as follows:

$$\beta_1 = b_1(1 + \theta_1 \sin(2\pi(t - \phi_1)))\alpha(t) \quad (S23)$$

$$\beta_2 = b_2(1 + \theta_2 \sin(2\pi(t - \phi_2)))\alpha(t) \quad (S24)$$

$$\lambda_1 = \beta_1(I_1 + J_1) \quad (S25)$$

$$\lambda_2 = \beta_2(I_2 + J_2) \quad (S26)$$

In Supplementary Figures S2–S4, we assumed the following parameters: $b_1 = 2 \times 52/\text{years}$, $b_2 = 4 \times 52/\text{years}$, $\phi_1 = \phi_2 = 0$, $\epsilon_{12} = 0.9$, $\epsilon_{21} = 0.5$, $\gamma_1 = \gamma_2 = 52/\text{years}$, $\delta_1 = \delta_2 = 1/\text{years}$, and $\mu = 1/70/\text{years}$. For all simulations, we assumed a 50% transmission reduction for 6 months from 2020:

$$\alpha(t) = \begin{cases} 0.5 & 2020 \leq t < 2020.5 \\ 1 & \text{otherwise} \end{cases} \quad (S27)$$

The seasonal amplitude θ is varied from 0 to 0.4. All simulations were run from 1900 to 2030 with following initial conditions: $S(0) = 1 - 2 \times 10^{-6}$, $I_1(0) = 1 \times 10^{-6}$, $I_2(0) = 1 \times 10^{-6}$, $R_1(0) = 0$, $R_2(0) = 0$, $J_1(0) = 0$, $J_2(0) = 0$, and $R(0) = 0$.

We considered three scenarios for measuring pathogen resilience: (1) we only have information about strain 1, (2) we only have information about strain 2, and (3) we are unable to distinguish between strains. In the first two scenarios (see panels A–C for strain 1 and panels D–F for strain 2), we considered the dynamics of average

⁷³² susceptibility for each strain and total prevalence:

$$\bar{S}_1 = S + \epsilon_{12}R_2 \quad (\text{S28})$$

$$\hat{I}_1 = I_1 + J_1 \quad (\text{S29})$$

$$\bar{S}_2 = S + \epsilon_{21}R_1 \quad (\text{S30})$$

$$\hat{I}_2 = I_2 + J_2 \quad (\text{S31})$$

⁷³³ In the third scenario (panels G–I), we considered the dynamics of total susceptible
⁷³⁴ and infected populations:

$$\hat{S} = S + R_2 + R_1 \quad (\text{S32})$$

$$\hat{I} = I_1 + J_1 + I_2 + J_2 \quad (\text{S33})$$

⁷³⁵ These quantities were used to compute the normalized distance from the attractor,
⁷³⁶ as described in the main text.

⁷³⁷ Estimating intrinsic resilience using a mechanistic model

⁷³⁸ We tested whether we can reliably estimate the intrinsic resilience of a system by fit-
⁷³⁹ ting a mechanistic model. Specifically, we simulated case time series from stochastic
⁷⁴⁰ SIRS and two-strain models and fitted a simple, deterministic SIRS model using a
⁷⁴¹ Bayesian framework [4, 23, 48].

⁷⁴² We simulated the models in discrete time with a daily time step ($\Delta t = 1$),
⁷⁴³ incorporating demographic stochasticity:

$$\beta(t) = \mathcal{R}_0 \left(1 + \theta \cos \left(\frac{2\pi t}{364} \right) \right) \alpha(t)(1 - \exp(-\gamma)) \quad (\text{S34})$$

$$\text{FOI}(t) = \beta(t)I(t - \Delta t)/N \quad (\text{S35})$$

$$B(t) \sim \text{Poisson}(\mu N) \quad (\text{S36})$$

$$\Delta S(t) \sim \text{Binom}(S(t - \Delta t), 1 - \exp(-(\text{FOI}(t) + \mu)\Delta t)) \quad (\text{S37})$$

$$N_{SI}(t) \sim \text{Binom}\left(\Delta S(t), \frac{\text{FOI}(t)}{\text{FOI}(t) + \mu}\right) \quad (\text{S38})$$

$$\Delta I(t) \sim \text{Binom}(I(t - \Delta t), 1 - \exp(-(\gamma + \mu)\Delta t)) \quad (\text{S39})$$

$$N_{IR}(t) \sim \text{Binom}\left(\Delta I(t), \frac{\gamma}{\gamma + \mu}\right) \quad (\text{S40})$$

$$\Delta R(t) \sim \text{Binom}(R(t - \Delta t), 1 - \exp(-(\delta + \mu)\Delta t)) \quad (\text{S41})$$

$$N_{RS}(t) \sim \text{Binom}\left(\Delta R(t), \frac{\delta}{\delta + \mu}\right) \quad (\text{S42})$$

$$S(t) = S(t - \Delta t) + N_{RS}(t) + B(t) - \Delta S(t) \quad (\text{S43})$$

$$I(t) = I(t - \Delta t) + N_{SI}(t) - \Delta I(t) \quad (\text{S44})$$

$$R(t) = R(t - \Delta t) + N_{IR}(t) - \Delta R(t) \quad (\text{S45})$$

744 where FOI represents the force of infection; N_{ij} represents the number of individuals
 745 moving from compartment i to j on a given day; and $B(t)$ represents the number
 746 of new births. All other parameters definitions can be found in the description of
 747 the deterministic version of the model. We simulated the model on a daily scale—
 748 assuming 364 days in a year so that it can be evenly grouped into 52 weeks—with
 749 the following parameters: $\mathcal{R}_0 = 3$, $\theta = 0.1$, $\gamma = 1/7/\text{days}$, $\delta = 1/(364 \times 2)/\text{days}$,
 750 $\mu = 1/(364 \times 50)/\text{days}$, and $N = 1 \times 10^8$. The model was simulated from 1900 to
 751 2030 assuming $S(0) = N/3$, $I(0) = 100$, and $R(0) = N - S(0) - I(0)$. The observed
 752 incidence from the model was then simulated as follows:

$$C(t) = \text{Beta-Binom}(N_{SI}(t), \rho, k), \quad (\text{S46})$$

753 where ρ represents the reporting probability and k represents the overdispersion
 754 parameter of beta-binomial distribution. Here, we used the beta-binomial distribu-
 755 tion to account for overdispersion in reporting. We assumed $\rho = 0.002$ (i.e., 0.2%
 756 probability) and $k = 1000$.

757 We used an analogous approach for the two-strain model:

$$\beta_1(t) = b_1 \left(1 + \theta_1 \cos \left(\frac{2\pi(t - \phi_1)}{364} \right) \right) \alpha(t) \quad (\text{S47})$$

$$\beta_2(t) = b_2 \left(1 + \theta_2 \cos \left(\frac{2\pi(t - \phi_2)}{364} \right) \right) \alpha(t) \quad (\text{S48})$$

$$\text{FOI}_1(t) = \beta_1(t)(I_1(t - \Delta t) + J_1(t - \Delta t))/N \quad (\text{S49})$$

$$\text{FOI}_2(t) = \beta_2(t)(I_2(t - \Delta t) + J_2(t - \Delta t))/N \quad (\text{S50})$$

$$B(t) \sim \text{Poisson}(\mu N) \quad (\text{S51})$$

$$\Delta S(t) \sim \text{Binom}(S(t - \Delta t), 1 - \exp(-(\text{FOI}_1(t) + \text{FOI}_2(t) + \mu)\Delta t)) \quad (\text{S52})$$

$$N_{SI_1}(t) \sim \text{Binom}\left(\Delta S(t), \frac{\text{FOI}_1(t)}{\text{FOI}_1(t) + \text{FOI}_2(t) + \mu}\right) \quad (\text{S53})$$

$$N_{SI_2}(t) \sim \text{Binom}\left(\Delta S(t), \frac{\text{FOI}_2(t)}{\text{FOI}_1(t) + \text{FOI}_2(t) + \mu}\right) \quad (\text{S54})$$

$$\Delta I_1(t) \sim \text{Binom}(I_1(t - \Delta t), 1 - \exp(-(\gamma_1 + \mu)\Delta t)) \quad (\text{S55})$$

$$N_{I_1 R_1}(t) \sim \text{Binom}\left(\Delta I_1(t), \frac{\gamma_1}{\gamma_1 + \mu}\right) \quad (\text{S56})$$

$$\Delta I_2(t) \sim \text{Binom}(I_2(t - \Delta t), 1 - \exp(-(\gamma_2 + \mu)\Delta t)) \quad (\text{S57})$$

$$N_{I_2 R_2}(t) \sim \text{Binom}\left(\Delta I_2(t), \frac{\gamma_2}{\gamma_2 + \mu}\right) \quad (\text{S58})$$

$$\Delta R_1(t) \sim \text{Binom}(R_1(t - \Delta t), 1 - \exp(-(\epsilon_{21}\text{FOI}_2(t) + \rho_1 + \mu)\Delta t)) \quad (\text{S59})$$

$$N_{R_1 S}(t) \sim \text{Binom}\left(\Delta R_1(t), \frac{\rho_1}{\epsilon_{21}\text{FOI}_2(t) + \rho_1 + \mu}\right) \quad (\text{S60})$$

$$N_{R_1 J_2}(t) \sim \text{Binom}\left(\Delta R_1(t), \frac{\epsilon_{21}\text{FOI}_2(t)}{\epsilon_{21}\text{FOI}_2(t) + \rho_1 + \mu}\right) \quad (\text{S61})$$

$$\Delta R_2(t) \sim \text{Binom}(R_2(t - \Delta t), 1 - \exp(-(\epsilon_{12}\text{FOI}_1(t) + \rho_2 + \mu)\Delta t)) \quad (\text{S62})$$

$$N_{R_2S}(t) \sim \text{Binom}\left(\Delta R_2(t), \frac{\rho_2}{\epsilon_{12}\text{FOI}_1(t) + \rho_2 + \mu}\right) \quad (\text{S63})$$

$$N_{R_2J_1}(t) \sim \text{Binom}\left(\Delta R_2(t), \frac{\epsilon_{12}\text{FOI}_1(t)}{\epsilon_{12}\text{FOI}_1(t) + \rho_2 + \mu}\right) \quad (\text{S64})$$

$$\Delta J_1(t) \sim \text{Binom}(J_1(t - \Delta t), 1 - \exp(-(\gamma_1 + \mu)\Delta t)) \quad (\text{S65})$$

$$N_{J_1R}(t) \sim \text{Binom}\left(\Delta J_1(t), \frac{\gamma_1}{\gamma_1 + \mu}\right) \quad (\text{S66})$$

$$\Delta J_2(t) \sim \text{Binom}(J_2(t - \Delta t), 1 - \exp(-(\gamma_2 + \mu)\Delta t)) \quad (\text{S67})$$

$$N_{J_2R}(t) \sim \text{Binom}\left(\Delta J_2(t), \frac{\gamma_2}{\gamma_2 + \mu}\right) \quad (\text{S68})$$

$$\Delta R(t) \sim \text{Binom}(R(t - \Delta t), 1 - \exp(-(\rho_1 + \rho_2 + \mu)\Delta t)) \quad (\text{S69})$$

$$N_{RR_1}(t) \sim \text{Binom}\left(\Delta R(t), \frac{\rho_1}{\rho_1 + \rho_2 + \mu}\right) \quad (\text{S70})$$

$$N_{RR_2}(t) \sim \text{Binom}\left(\Delta R(t), \frac{\rho_2}{\rho_1 + \rho_2 + \mu}\right) \quad (\text{S71})$$

$$S(t) = S(t - \Delta t) - \Delta S(t) + B(t) + N_{R_1S}(t) + N_{R_2S}(t) \quad (\text{S72})$$

$$I_1(t) = I_1(t - \Delta t) - \Delta I_1(t) + N_{SI_1}(t) \quad (\text{S73})$$

$$I_2(t) = I_2(t - \Delta t) - \Delta I_2(t) + N_{SI_2}(t) \quad (\text{S74})$$

$$R_1(t) = R_1(t - \Delta t) - \Delta R_1(t) + N_{I_1R_1}(t) + N_{RR_1}(t) \quad (\text{S75})$$

$$R_2(t) = R_2(t - \Delta t) - \Delta R_2(t) + N_{I_2R_2}(t) + N_{RR_2}(t) \quad (\text{S76})$$

$$J_1(t) = J_1(t - \Delta t) - \Delta J_1(t) + N_{R_2J_1}(t) \quad (\text{S77})$$

$$J_2(t) = J_2(t - \Delta t) - \Delta J_2(t) + N_{R_1J_2}(t) \quad (\text{S78})$$

$$R(t) = R(t - \Delta t) - \Delta R(t) + N_{J_1R}(t) + N_{J_2R}(t) \quad (\text{S79})$$

We simulated the model on a daily scale with previously estimated parameters for the RSV-HMPV interaction [34]: $b_1 = 1.7/\text{weeks}$, $b_2 = 1.95/\text{weeks}$, $\theta_1 = 0.4$, $\theta_2 = 0.3$, $\phi_1 = 0.005 \times 7/364$, $\phi_2 = 4.99 \times 7/364$, $\epsilon_{12} = 0.92$, $\epsilon_{21} = 0.45$, $\gamma_1 = 1/10/\text{days}$, $\gamma_2 = 1/10/\text{days}$, $\rho_1 = 1/364/\text{days}$, $\rho_2 = 1/364/\text{days}$, $\mu = 1/(70 \times 364)/\text{days}$, and $N = 1 \times 10^8$. The model was simulated from 1900 to 2030 assuming $S(0) = N - 200$, $I_1(0) = 100$, $I_2(0) = 100$, $R_1(0) = 0$, $R_2(0) = 0$, $J_1(0) = 0$, $J_2(0) = 0$, and $R(0) = 0$. The observed incidence for each strain is then simulated as follows:

$$C_1(t) = \text{Beta-Binom}(N_{SI_1}(t) + N_{R_2J_1}, \rho, k), \quad (\text{S80})$$

$$C_2(t) = \text{Beta-Binom}(N_{SI_2}(t) + N_{R_1J_2}, \rho, k), \quad (\text{S81})$$

where ρ represents the reporting probability and k represents the overdispersion parameter of beta-binomial distribution. We assumed $\rho = 0.002$ (i.e., 0.2% probability) and $k = 500$. We also considered the total incidence: $C_{\text{total}}(t) = C_1(t) + C_2(t)$.

For both models, we considered a more realistically shaped pandemic perturbation $\alpha(t)$ to challenge our ability to estimate the intervention effects. Thus, we

assumed a 40% transmission reduction for 3 months from March 2020, followed by a 10% transmission reduction for 6 months, 20% transmission reduction for 3 months, and a final return to normal levels:

$$\alpha(t) = \begin{cases} 1 & t < 2020.25 \\ 0.6 & 2020.25 \leq t < 2020.5 \\ 0.9 & 2020.5 \leq t < 2021 \\ 0.8 & 2021 \leq t < 2021.25 \\ 1 & 2021.25 \leq t \end{cases}. \quad (\text{S82})$$

For all simulations, we truncated the time series from the beginning of 2014 to the end of 2023 and aggregated them into weekly cases.

To infer intrinsic resilience from time series, we fitted a simple discrete time, deterministic SIRS model in a Bayesian framework [4]:

$$\Delta t = 1 \text{ week} \quad (\text{S83})$$

$$\text{FOI}(t) = \beta(t)(I(t - \Delta t) + \omega)/N \quad (\text{S84})$$

$$\Delta S(t) = [1 - \exp(-(\text{FOI}(t) + \mu)\Delta t)] S(t - \Delta t) \quad (\text{S85})$$

$$N_{SI}(t) = \frac{\text{FOI}(t)\Delta S(t)}{\text{FOI}(t) + \mu} \quad (\text{S86})$$

$$\Delta I(t) = [1 - \exp(-(\gamma + \mu)\Delta t)] I(t - \Delta t) \quad (\text{S87})$$

$$N_{IR}(t) = \frac{\gamma \Delta I(t)}{\gamma + \mu} \quad (\text{S88})$$

$$\Delta R(t) = [1 - \exp(-(\nu + \mu)\Delta t)] R(t - \Delta t) \quad (\text{S89})$$

$$N_{RS}(t) = \frac{\nu \Delta R(t)}{\nu + \mu} \quad (\text{S90})$$

$$S(t) = S(t - \Delta t) + \mu S - \Delta S(t) + N_{RS}(t) \quad (\text{S91})$$

$$I(t) = I(t - \Delta t) - \Delta I(t) + N_{SI}(t) \quad (\text{S92})$$

$$R(t) = R(t - \Delta t) - \Delta R(t) + N_{IR}(t) \quad (\text{S93})$$

where we include an extra term ω to account for importation. Although actual simulations did not include any importation, we had found that including this term generally helped with model convergence in previous analyses [4]. The transmission rate was divided into a seasonal term $\beta_{\text{seas}}(t)$ (repeated every year) and intervention term $\alpha(t)$, which were estimated jointly:

$$\beta(t) = \beta_{\text{seas}}(t)\alpha(t), \quad (\text{S94})$$

where $\alpha < 1$ corresponds to reduction in transmission due to intervention effects. To constrain the smoothness of $\beta_{\text{seas}}(t)$, we imposed cyclic, random-walk priors:

$$\beta_{\text{seas}}(t) \sim \text{Normal}(\beta_{\text{seas}}(t - 1), \sigma) \quad t = 2 \dots 52 \quad (\text{S95})$$

$$\beta_{\text{seas}}(1) \sim \text{Normal}(\beta_{\text{seas}}(52), \sigma) \quad (\text{S96})$$

$$\sigma \sim \text{Half-Normal}(0, 1) \quad (\text{S97})$$

⁷⁸⁴ We fixed $\alpha(t) = 1$ for all $t < 2020$ and estimate α assuming a normal prior:

$$\alpha \sim \text{Normal}(1, 0.25). \quad (\text{S98})$$

⁷⁸⁵ We assumed weakly informative priors on ω and ν :

$$\omega \sim \text{Half-Normal}(0, 200) \quad (\text{S99})$$

$$\nu \sim \text{Normal}(104, 26) \quad (\text{S100})$$

⁷⁸⁶ We assumed that the true birth/death rates, population sizes, and recovery rates
⁷⁸⁷ are known. We note, however, that assuming $\gamma = 1/\text{week}$ actually corresponds to
⁷⁸⁸ a mean simulated infectious period of 1.6 weeks due to a time discretization, which
⁷⁸⁹ is much longer than the true value; this approximation allows us to test whether we
⁷⁹⁰ can still robustly estimate the intrinsic resilience given parameter mis-specification.
⁷⁹¹ Initial conditions were estimated with following priors:

$$S(0) = Ns(0) \quad (\text{S101})$$

$$I(0) = Ni(0) \quad (\text{S102})$$

$$s(0) \sim \text{Uniform}(0, 1) \quad (\text{S103})$$

$$i(0) \sim \text{Half-Normal}(0, 0.001) \quad (\text{S104})$$

⁷⁹² Finally, the observation model was specified as follows:

$$\text{Cases}(t) \sim \text{Negative-Binomial}(\rho N_{SI}(t), \phi) \quad (\text{S105})$$

$$\rho \sim \text{Half-Normal}(0, 0.02) \quad (\text{S106})$$

$$\phi \sim \text{Half-Normal}(0, 10) \quad (\text{S107})$$

⁷⁹³ where ρ represents the reporting probability and ϕ represents the negative binomial
⁷⁹⁴ overdispersion parameter.

⁷⁹⁵ The model was fitted to four separate time series: (1) incidence time series from
⁷⁹⁶ the SIRS model, (2) incidence time series for strain 1 from the two-strain model,
⁷⁹⁷ (3) incidence time series for strain 2 from the two-strain model, and (4) combined
⁷⁹⁸ incidence time series for strains 1 and 2 from the two-strain model. The model
⁷⁹⁹ was fitted using rstan [49, 50] with 4 chains, each consisting of 2000 iterations.
⁸⁰⁰ The resulting posterior distribution was used to calculate the intrinsic resilience of
⁸⁰¹ the seasonally unforced SIRS model with the same parameters; eigenvalues of the
⁸⁰² discrete-time SIR model were computed by numerically finding the equilibrium and
⁸⁰³ calculating the Jacobian matrix.

804 **Validations for window-selection criteria**

805 We used stochastic SIRS simulations to identify optimal parameters for the window-
 806 selection criteria that we used for the linear regression for estimating empirical re-
 807 silience. For each simulation, we began by generating a random perturbation $\alpha(t)$
 808 from a random set of parameters. First, we drew the duration of perturbation τ_{npi}
 809 from a uniform distribution between 1 and 2 years. Then, we drew independent
 810 normal variables z_i of length $[364\tau_{\text{npi}}]$ with a standard deviation of 0.02 and took a
 811 reverse cumulative sum to obtain a realistic shape for the perturbation:

$$x_n = 1 + \sum_{i=n}^{[364\tau_{\text{npi}}]} z_i, \quad n = 1, \dots, [364\tau_{\text{npi}}]. \quad (\text{S108})$$

812 In contrast to simple perturbations that assume a constant reduction in transmis-
 813 sion, this approach allows us to model transmission reduction that varies over time
 814 smoothly. We repeated this random generation process until less than 10% of x_n
 815 exceeds 1—this was done to ensure the perturbation term $\alpha(t)$ stays below 1 (and
 816 therefore reduce transmission) for the most part. Then, we set any values that are
 817 above 1 or below 0 to 1 and 0, respectively. Then, we randomly drew the minimum
 818 transmission during perturbation α_{\min} from a uniform distribution between 0.5 and
 819 0.7 and scale x_n to have a minimum of α_{\min} :

$$x_{\text{scale},n} = \alpha_{\min} + (1 - \alpha_{\min}) \times \frac{x_n - \min x_n}{1 - \min x_n}. \quad (\text{S109})$$

820 This allowed us to simulate a realistically shaped perturbation:

$$\alpha(t) = \begin{cases} 1 & t < 2020 \\ x_{\text{scale},364(t-2020)} & 2020 \leq t < 2020 + \tau_{\text{npi}} \\ 1 & \tau_{\text{npi}} \leq t \end{cases}. \quad (\text{S110})$$

821 Given this perturbation function, we draw \mathcal{R}_0 from a uniform distribution between
 822 1.5 and 4 and the mean duration of immunity $1/\delta$ from a uniform distribution be-
 823 tween 1 and 4. Then, we simulate the stochastic SIRS model from $S(0) = 10^8/\mathcal{R}_0$
 824 and $I(0) = 100$ from 1990 to 2025 and truncate the time series to 2014–2025; if the
 825 epidemic becomes extinct before the end of simulation, we discard that simulation
 826 and start over from the perturbation generation step.

827 For each epidemic simulation, we computed the empirical resilience by varying
 828 the threshold R for the nearest neighbor approach from 4 to 14 with increments of
 829 2, the number of divisions K for the window selection between 8 and 25, and the
 830 truncation threshold a for the window selection between 1 to 3; this was done for all
 831 possible combinations of R , K , and a . We also compared this with the naive approach
 832 that uses the entire distance-from-attractor time series, starting from the maximum
 833 distance to the end of the time series. We repeated this procedure 500 times and
 834 quantified the correlation between empirical and intrinsic resilience estimates across
 835 two approaches.

Supplementary Figures

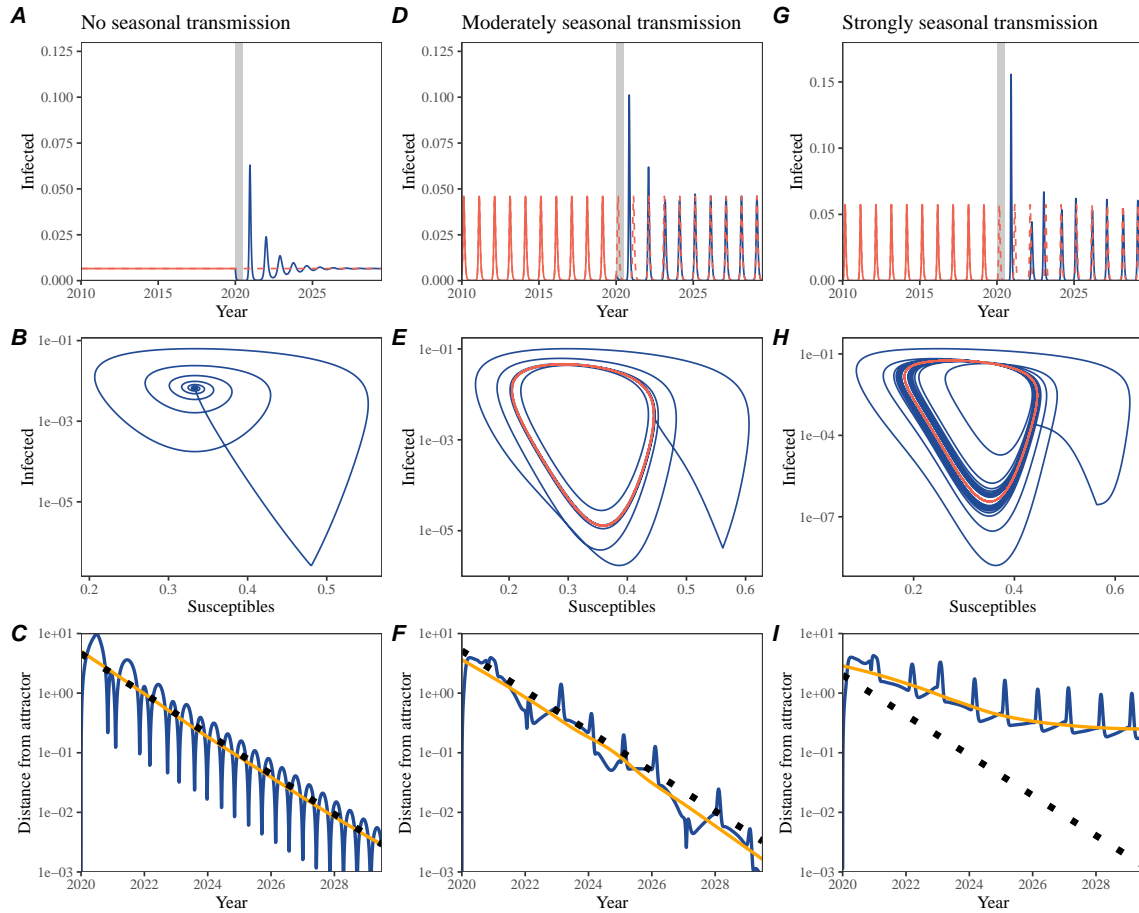


Figure S1: Impact of seasonal transmission on pathogen resilience. (A, D, G) Simulated epidemic trajectories using the SIRS model without seasonal forcing (A), with seasonal forcing of amplitude of 0.2 (D), and with seasonal forcing of amplitude of 0.4 (G). Red and blue solid lines represent epidemic dynamics before and after interventions are introduced, respectively. Red dashed lines represent counterfactual epidemic dynamics in the absence of interventions. Gray regions indicate the duration of interventions. (B, E, H) Phase plane representation of the time series in panels A, D, and G alongside the corresponding susceptible host dynamics. Red and blue solid lines represent epidemic trajectories on an SI phase plane before and after interventions are introduced, respectively. (C, F, I) Changes in logged distance from the attractor over time. Blue lines represent the logged distance from the attractor. Orange lines represent the locally estimated scatterplot smoothing (LOESS) fits to the logged distance from the attractor. Dotted lines show the intrinsic resilience of the seasonally unforced system.

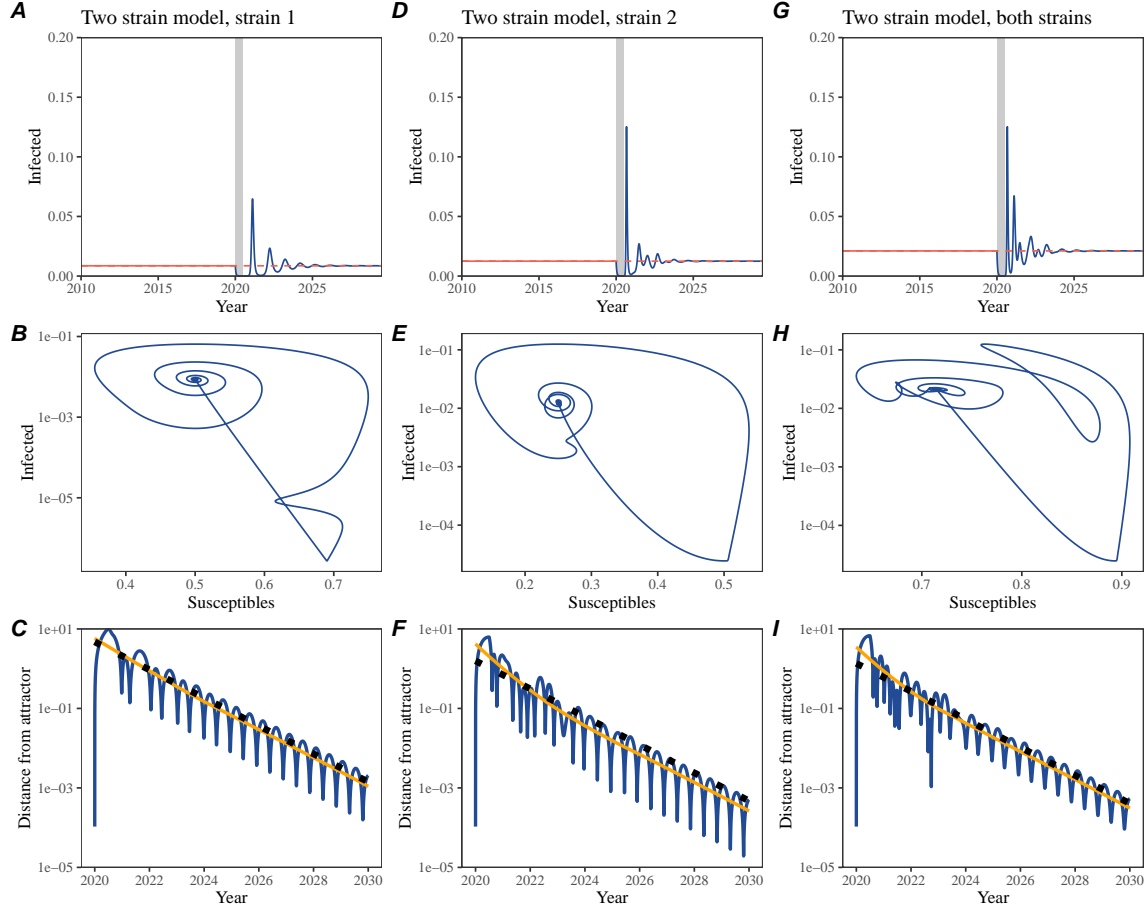


Figure S2: A simple method to measure pathogen resilience following pandemic perturbations for a two-strain competition system without seasonal forcing. (A, D, G) Simulated epidemic trajectories using a two-strain system without seasonal forcing. In this model, two strains compete through cross immunity. Red and blue solid lines represent epidemic dynamics before and after interventions are introduced, respectively. Red dashed lines represent counterfactual epidemic dynamics in the absence of interventions. Gray regions indicate the duration of interventions. (B, E, H) Phase plane representation of the time series in panels A, D, and G alongside the corresponding susceptible host dynamics. Blue solid lines represent epidemic trajectories on an SI phase plane before and after interventions. (C, F, I) Changes in logged distance from the attractor over time. Blue lines represent the logged distance from the attractor. Orange lines represent the locally estimated scatterplot smoothing (LOESS) fits to the logged distance from the attractor. Dotted lines show the intrinsic resilience of the seasonally unforced system.

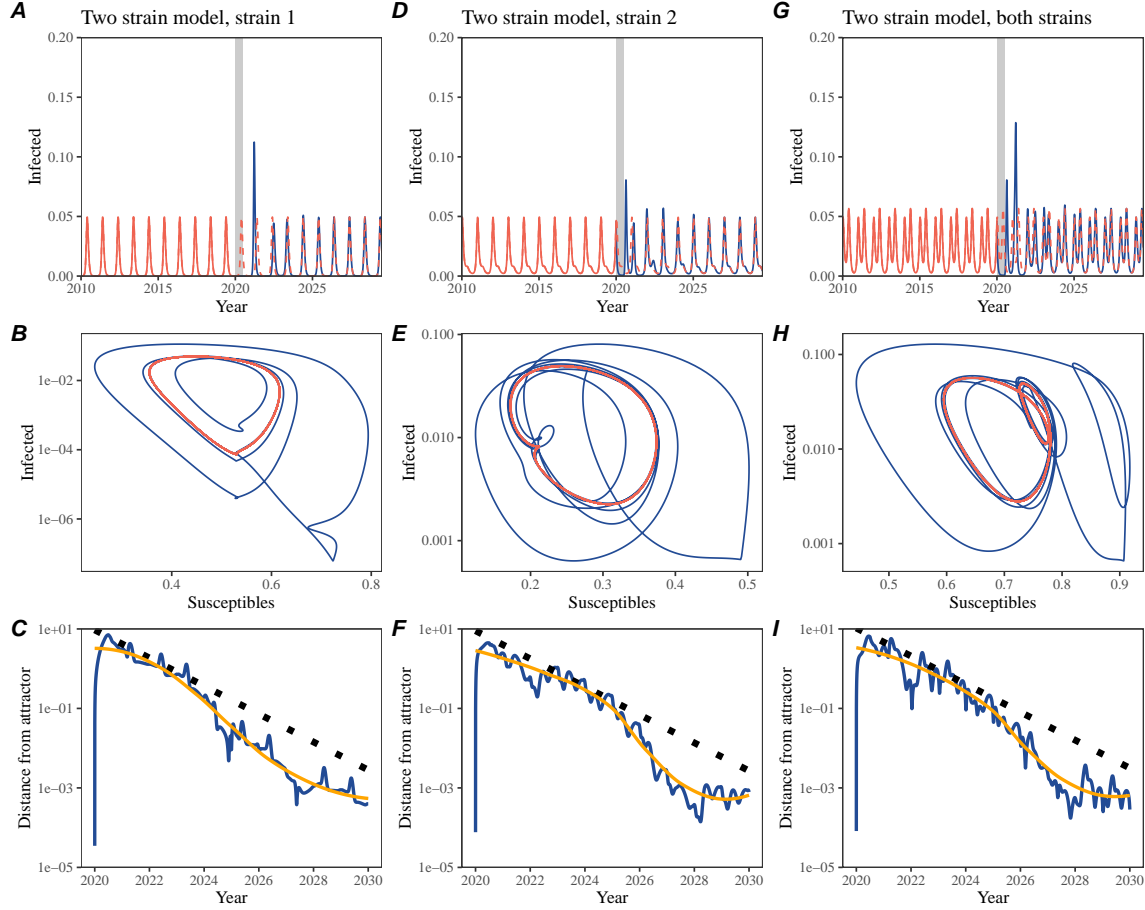


Figure S3: A simple method to measure pathogen resilience following pandemic perturbations for a two-strain competition system with seasonal forcing. (A, D, G) Simulated epidemic trajectories using a two-strain system with seasonal forcing (amplitude of 0.2). In this model, two strains compete through cross immunity. Red and blue solid lines represent epidemic dynamics before and after interventions are introduced, respectively. Red dashed lines represent counterfactual epidemic dynamics in the absence of interventions. Gray regions indicate the duration of interventions. (B, E, H) Phase plane representation of the time series in panels A, D, and G alongside the corresponding susceptible host dynamics. Red and blue solid lines represent epidemic trajectories on an SI phase plane before and after interventions are introduced, respectively. (C, F, I) Changes in logged distance from the attractor over time. Blue lines represent the logged distance from the attractor. Orange lines represent the locally estimated scatterplot smoothing (LOESS) fits to the logged distance from the attractor. Dotted lines show the intrinsic resilience of the seasonally unforced system.

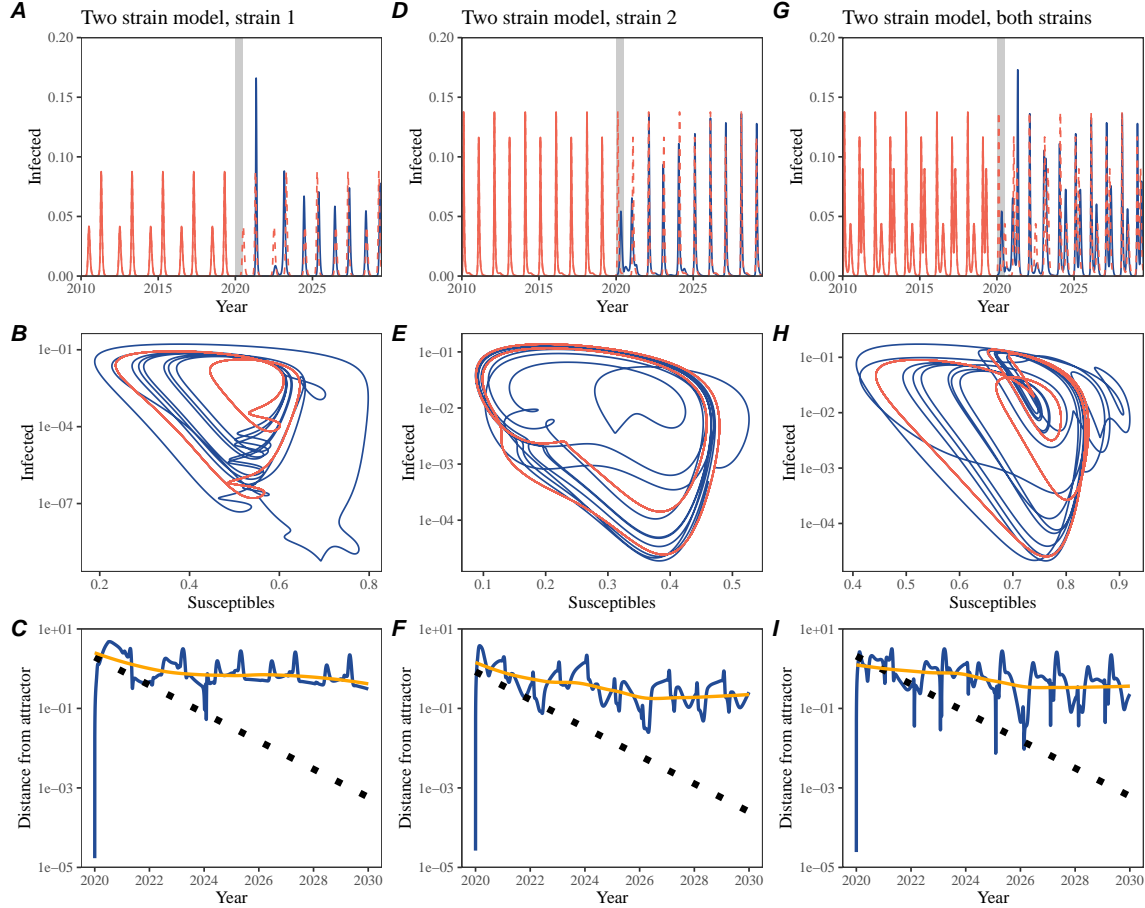


Figure S4: A simple method to measure pathogen resilience following pandemic perturbations for a multi-strain competition system with strong seasonal forcing. (A, D, G) Simulated epidemic trajectories using a two-strain system with seasonal forcing (amplitude of 0.2). In this model, two strains compete through cross immunity. Red and blue solid lines represent epidemic dynamics before and after interventions are introduced, respectively. Red dashed lines represent counterfactual epidemic dynamics in the absence of interventions. Gray regions indicate the duration of interventions. (B, E, H) Phase plane representation of the time series in panels A, D, and G alongside the corresponding susceptible host dynamics. Red and blue solid lines represent epidemic trajectories on an SI phase plane before and after interventions are introduced, respectively. (C, F, I) Changes in logged distance from the attractor over time. Blue lines represent the logged distance from the attractor. Orange lines represent the locally estimated scatterplot smoothing (LOESS) fits to the logged distance from the attractor. Dotted lines show the intrinsic resilience of the seasonally unforced system.

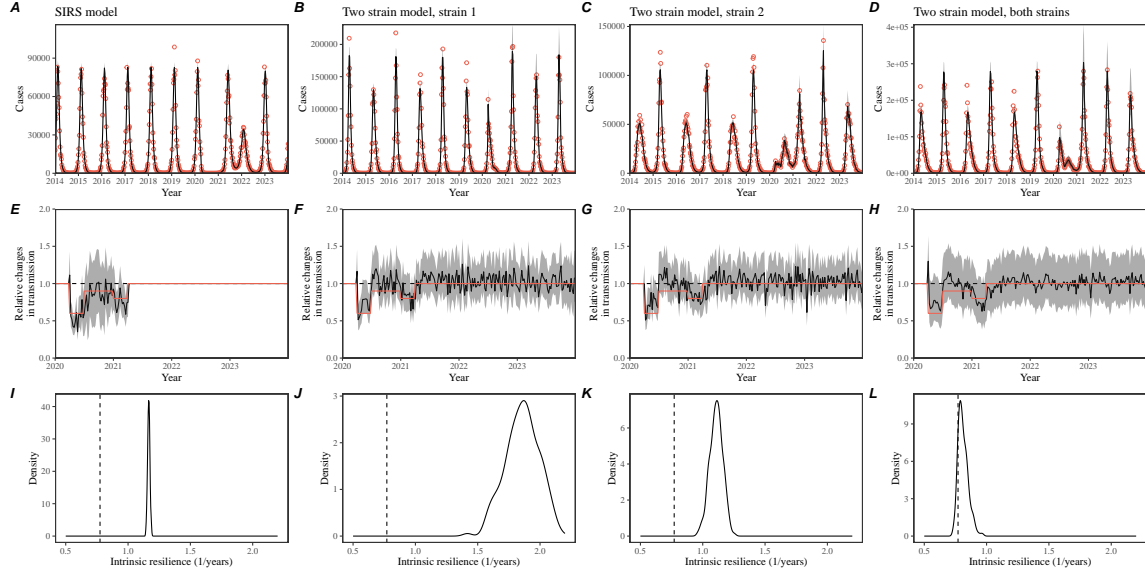


Figure S5: Mechanistic model fits to simulated data and inferred intrinsic resilience. We simulated discrete time, stochastic epidemic trajectories using a seasonally forced SIRS model (A,E,I) and a seasonally forced two-strain model (B–D, F–H, and J–L) and tested whether we can estimate the intrinsic resilience of the seasonally unforced versions of the model by fitting a mechanistic model (Supplementary Text). We fitted the same discrete time, one strain, deterministic SIRS model in each scenario. (A–D) Simulated case time series from corresponding models shown in the title (red) and SIRS model fits (black). (E–H) Assumed changes in transmission due to pandemic perturbations (red) and estimated time-varying relative transmission rates for the perturbation impact from the SIRS model fits (black). Solid lines and shaded regions represent fitted posterior median and 95% credible intervals. (I–L) Comparisons between the true and estimated intrinsic resilience of the seasonally unforced system. Vertical lines represent the true intrinsic resilience of the seasonally unforced system. Density plots represent the posterior distribution of the inferred intrinsic resilience of the seasonally unforced SIRS model using fitted parameters.

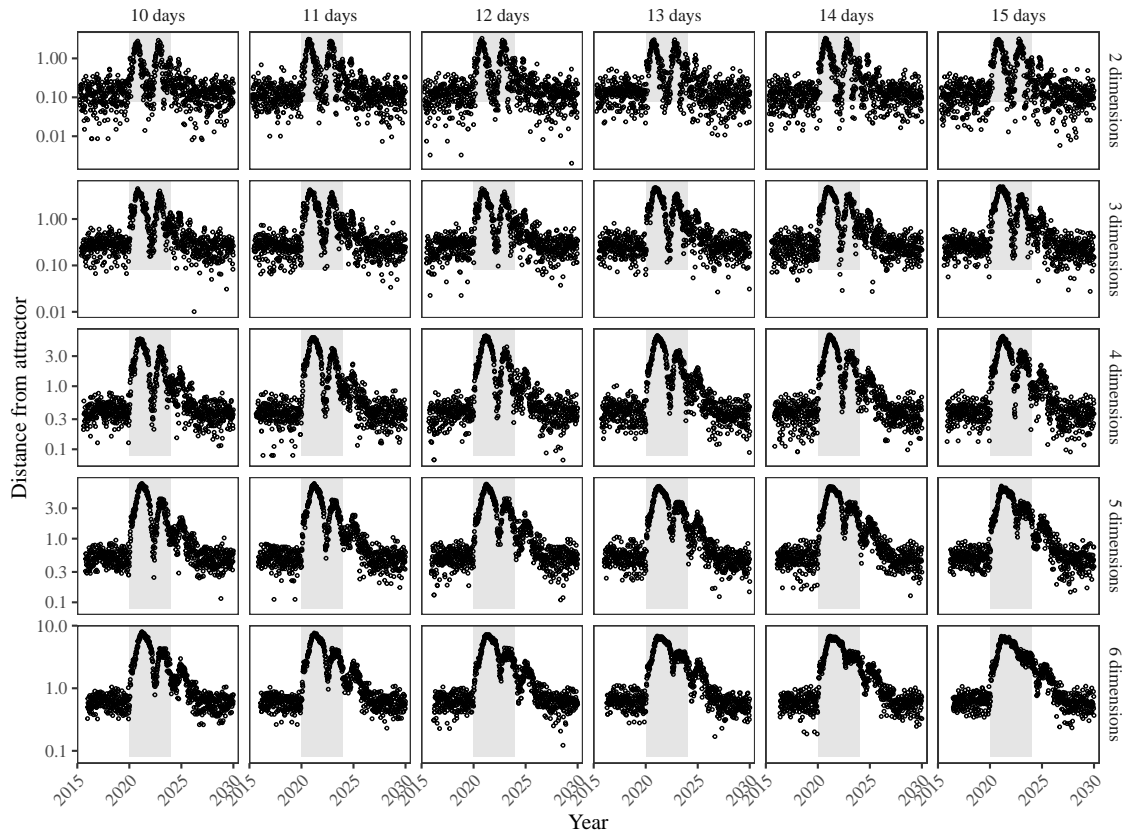


Figure S6: Sensitivity of the distance from the attractor to choice of embedding lags and dimensions. Sensitivity analysis for the distance-from-attractor time series shown in Figure 3E in the main text by varying the embedding lag between 10–15 days and embedding dimensions between 2–6 dimensions. The gray region represents the assumed period of pandemic perturbation.

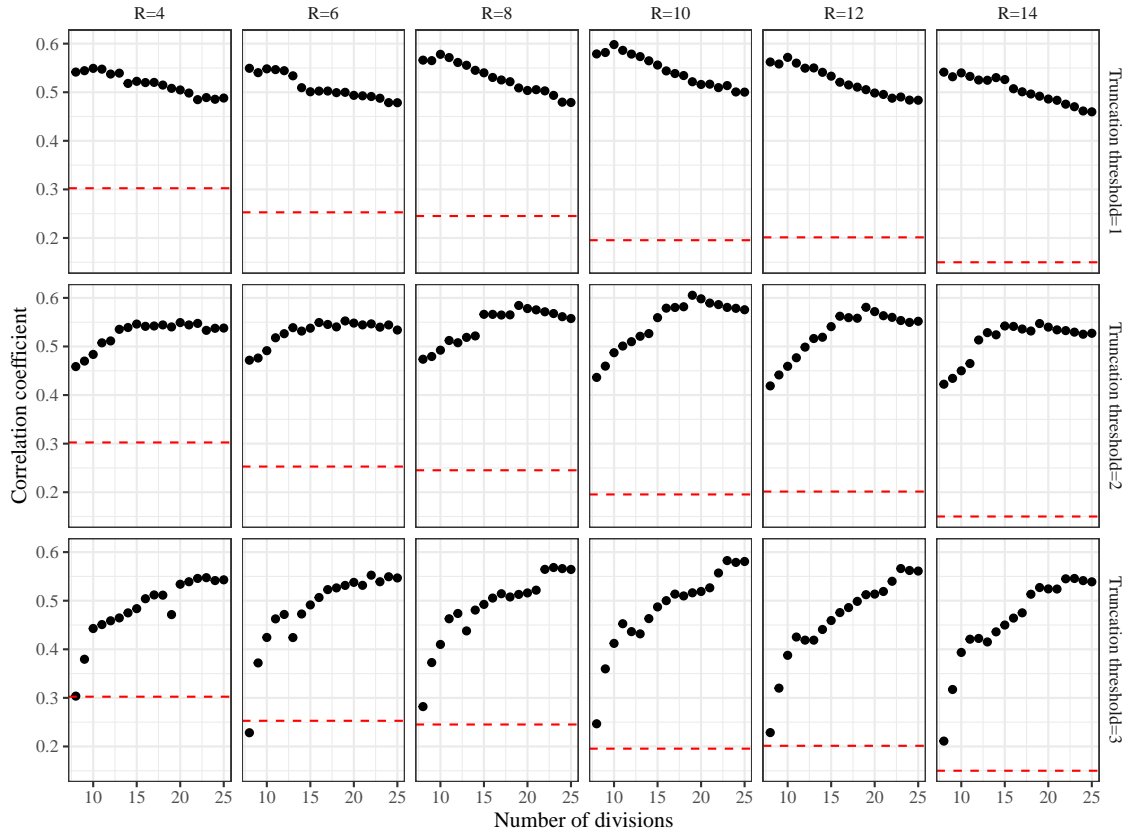


Figure S7: Impact of fitting window selection on the estimation of empirical resilience. We simulated 500 epidemics of a stochastic SIRS model with randomly drawn parameters and randomly generated pandemic perturbations (Supplementary Text). For each simulation, we varied the false nearest neighbor threshold R for reconstructing the empirical attractor as well as the parameters for regression window selection (i.e., the truncation threshold a and the number of divisions K). Each point represents the resulting correlation coefficient between empirical and intrinsic resilience estimates for a given scenario. Dashed lines represent the correlation coefficient between empirical and intrinsic resilience estimates for the naive approach that fits a linear regression on a log scale, starting from the maximum distance until the end of the time series.

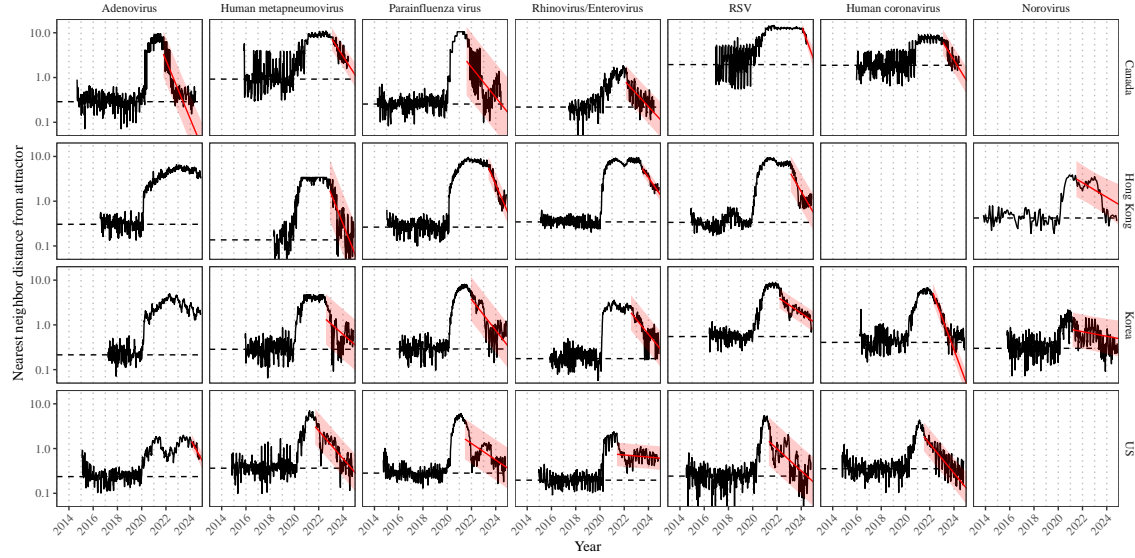


Figure S8: Estimated time series of distance from the attractor for each pathogen and corresponding linear regression fits using automated window selection criteria across Canada, Hong Kong, Korea, and the US. Black lines represent the estimated distance from the attractor. Red lines and shaded regions represent the linear regression fits and corresponding 95% confidence intervals. Dashed lines represent the average of the pre-pandemic nearest neighbor distances.

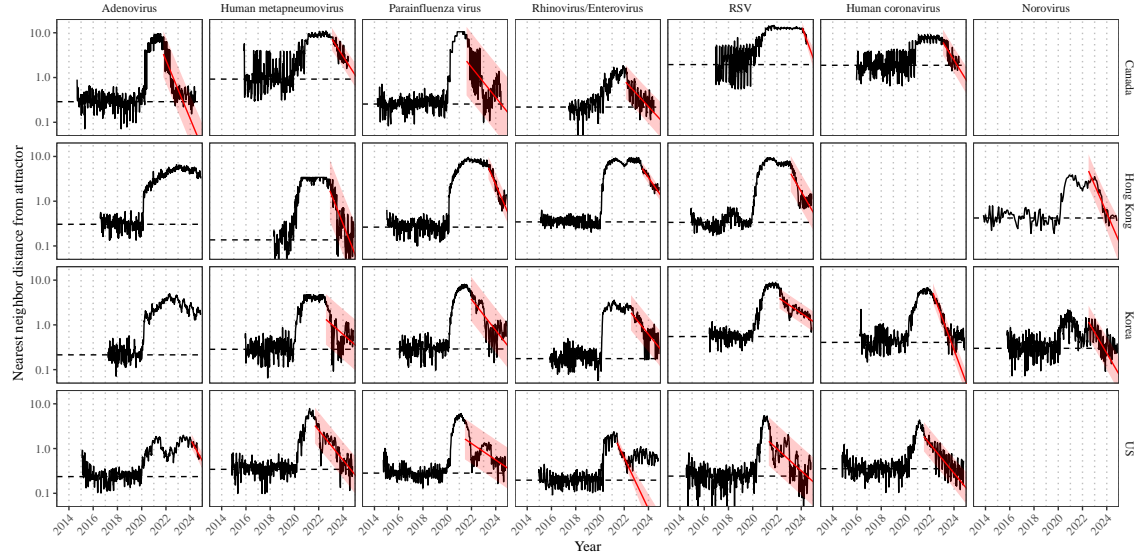


Figure S9: Estimated time series of distance from the attractor for each pathogen and corresponding linear regression fits across Canada, Hong Kong, Korea, and the US, including ad-hoc regression window selection. We used ad-hoc regression windows for norovirus in Hong Kong and Korea and rhinovirus/enterovirus in the US. Black lines represent the estimated distance from the attractor. Red lines and shaded regions represent the linear regression fits and corresponding 95% confidence intervals. Dashed lines represent the average of the pre-pandemic nearest neighbor distances.

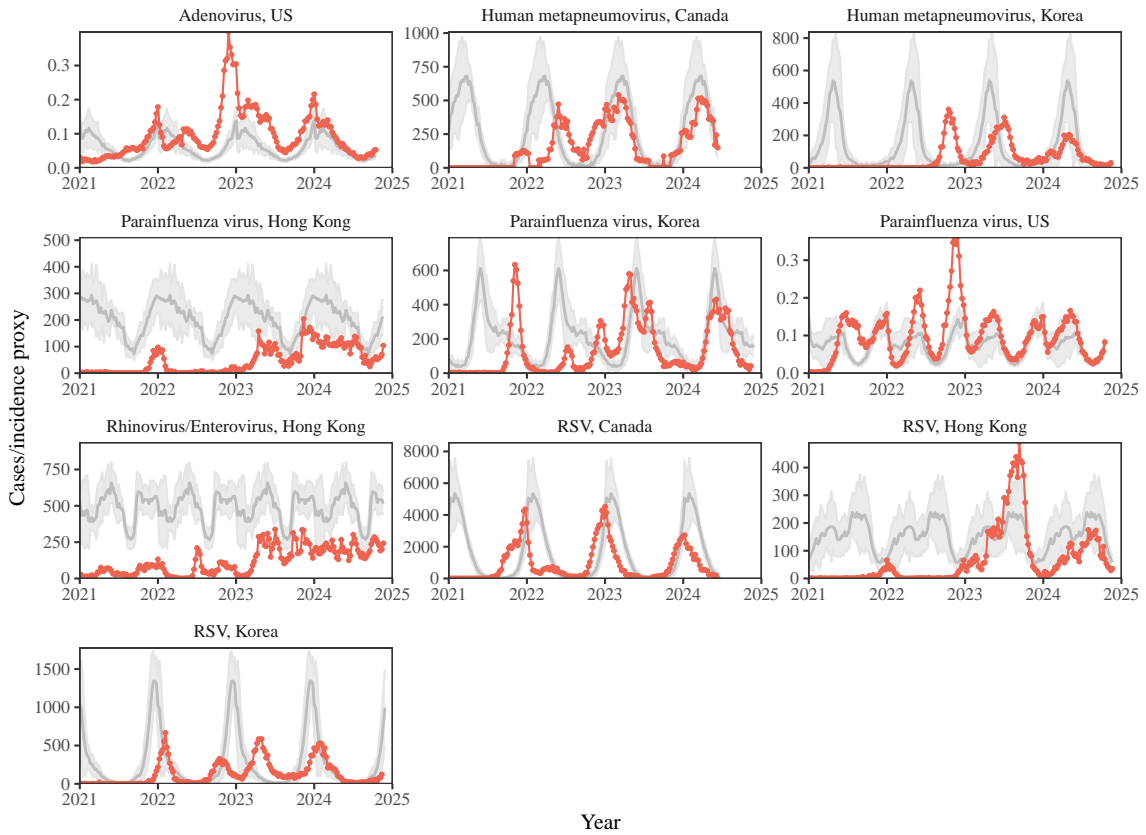


Figure S10: **Observed dynamics for pathogen that are predicted to return after the end of 2024.** Red points and lines represent data before 2020. Gray lines and shaded regions represent the mean seasonal patterns and corresponding 95% confidence intervals around the mean, previously shown in Figure 1.

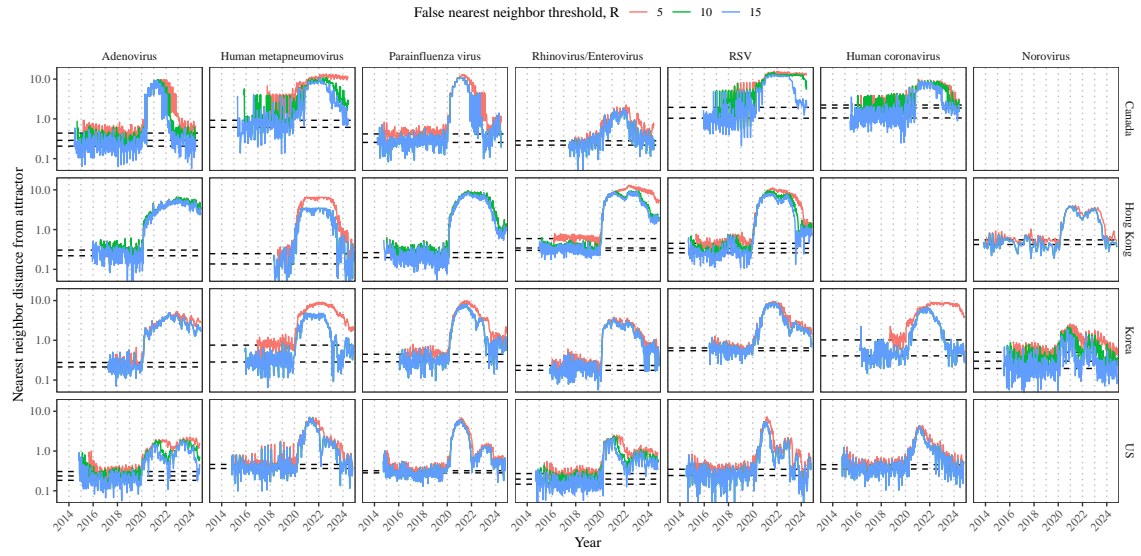


Figure S11: Estimated time series of distance from the attractor for each pathogen across different choices about false nearest neighbor threshold values. Using higher threshold values for the false nearest neighbor approach gives lower embedding dimensions. Colored lines represent the estimated distance from the attractor for different threshold values.

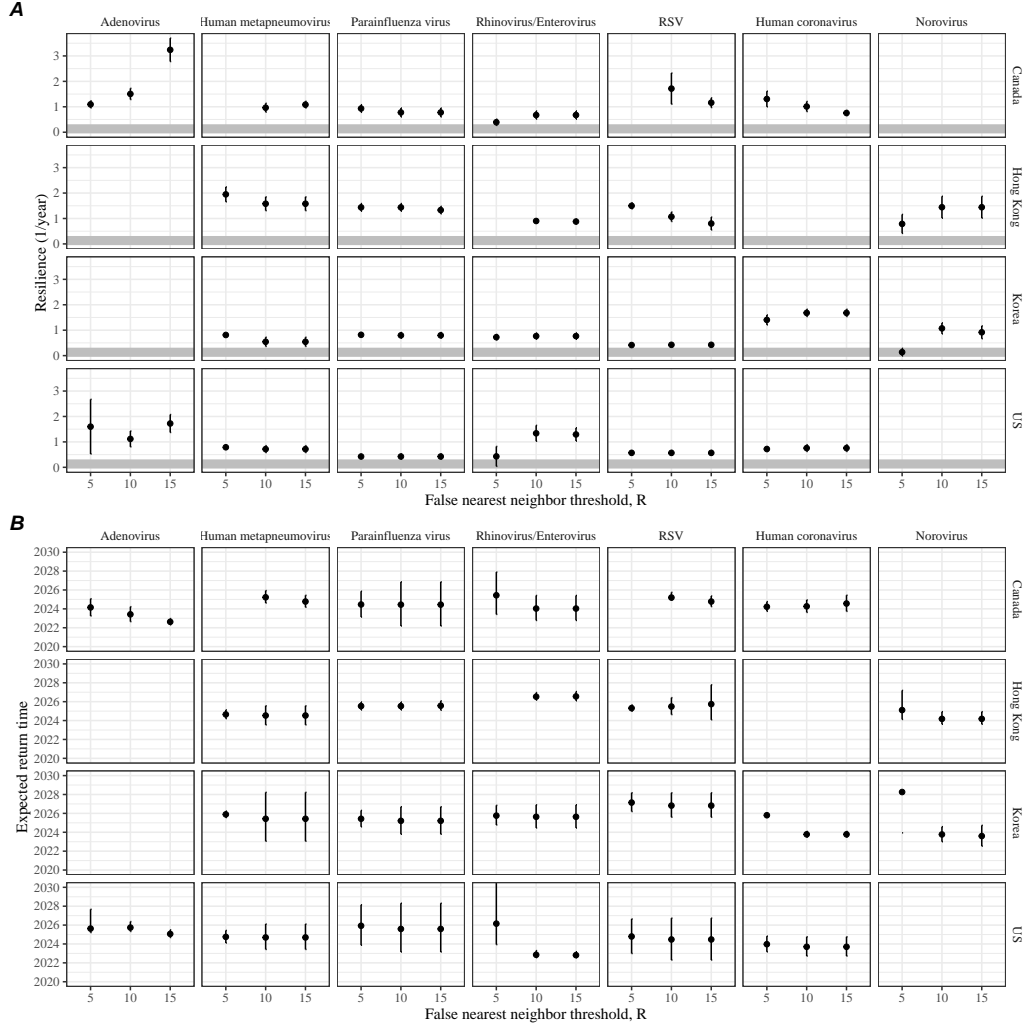


Figure S12: Summary of resilience estimates and predictions for return time across different choices about false nearest neighbor threshold values. The automated window selection method was used for all scenarios to estimate pathogen resilience, except for norovirus in Hong Kong and Korea and rhinovirus/enterovirus in the US. We used the same ad-hoc regression windows for norovirus in Hong Kong and Korea and rhinovirus/enterovirus in the US as we did in the main analysis. (A) Estimated pathogen resilience. The gray horizontal line represents the intrinsic resilience of pre-vaccination measles dynamics. (B) Predicted timing of when each pathogen will return to their pre-pandemic cycles. The dashed line in panel B indicates the end of 2024. Error bars represent 95% confidence intervals.

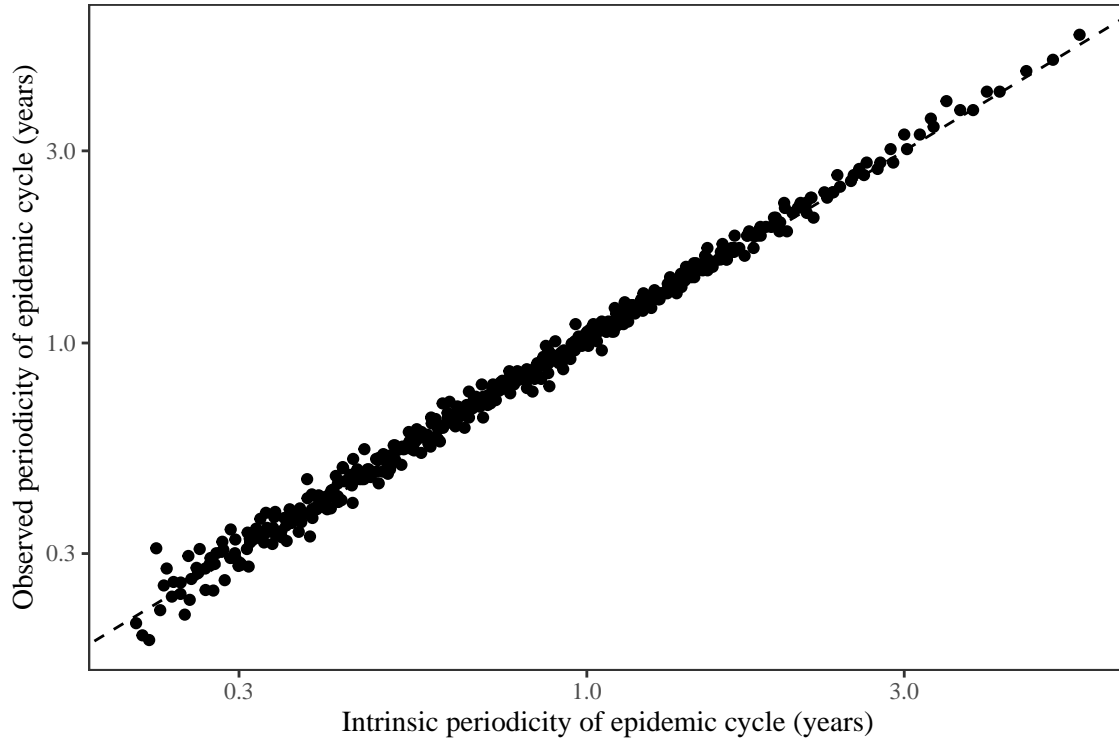


Figure S13: **Comparison between the observed and intrinsic periodicity of the epidemic cycle of the seasonally unforced SIRS model.** The observed periodicity of the epidemic corresponds to the periodicity at which maximum spectral density occurs. The intrinsic periodicity of the epidemic corresponds to $2\pi/\text{Im}(\lambda)$, where $\text{Im}(\lambda)$ is the imaginary part of the eigenvalue.

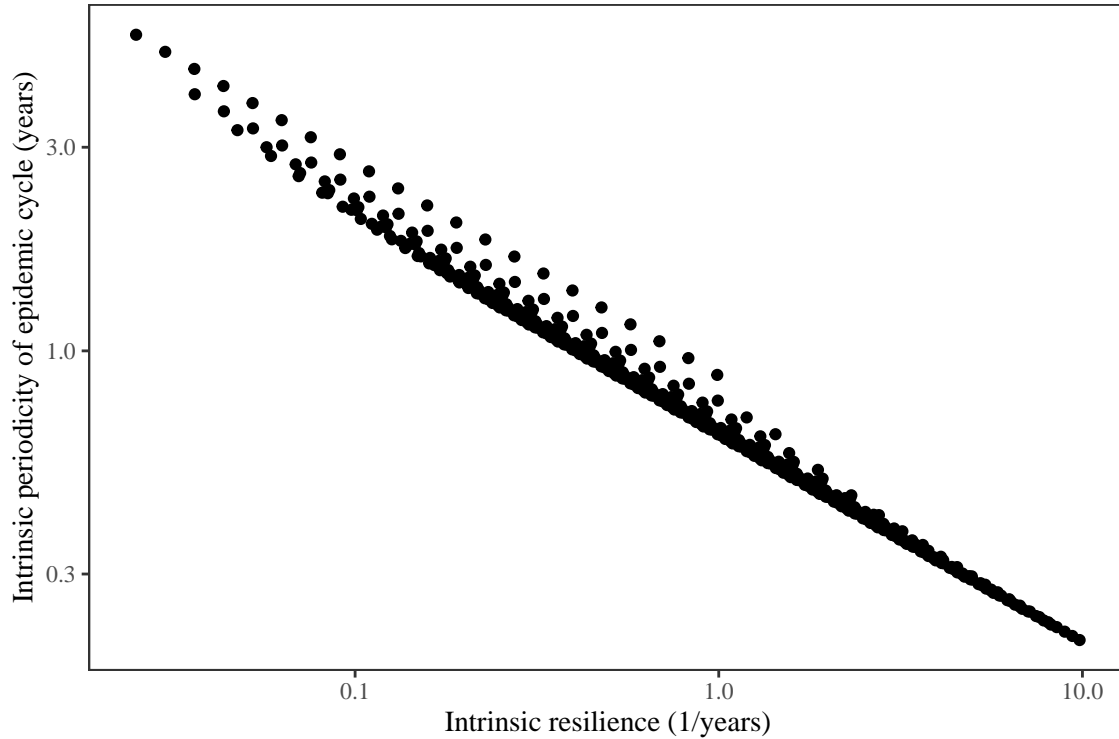


Figure S14: **Comparison between the intrinsic resilience and periodicity of the epidemic cycle of the seasonally unforced SIRS model.** The intrinsic resilience of the epidemic corresponds to the negative of the real value of the eigenvalue $-\text{Re}(\lambda)$. The intrinsic periodicity of the epidemic corresponds to $2\pi/\text{Im}(\lambda)$, where $\text{Im}(\lambda)$ is the imaginary part of the eigenvalue.

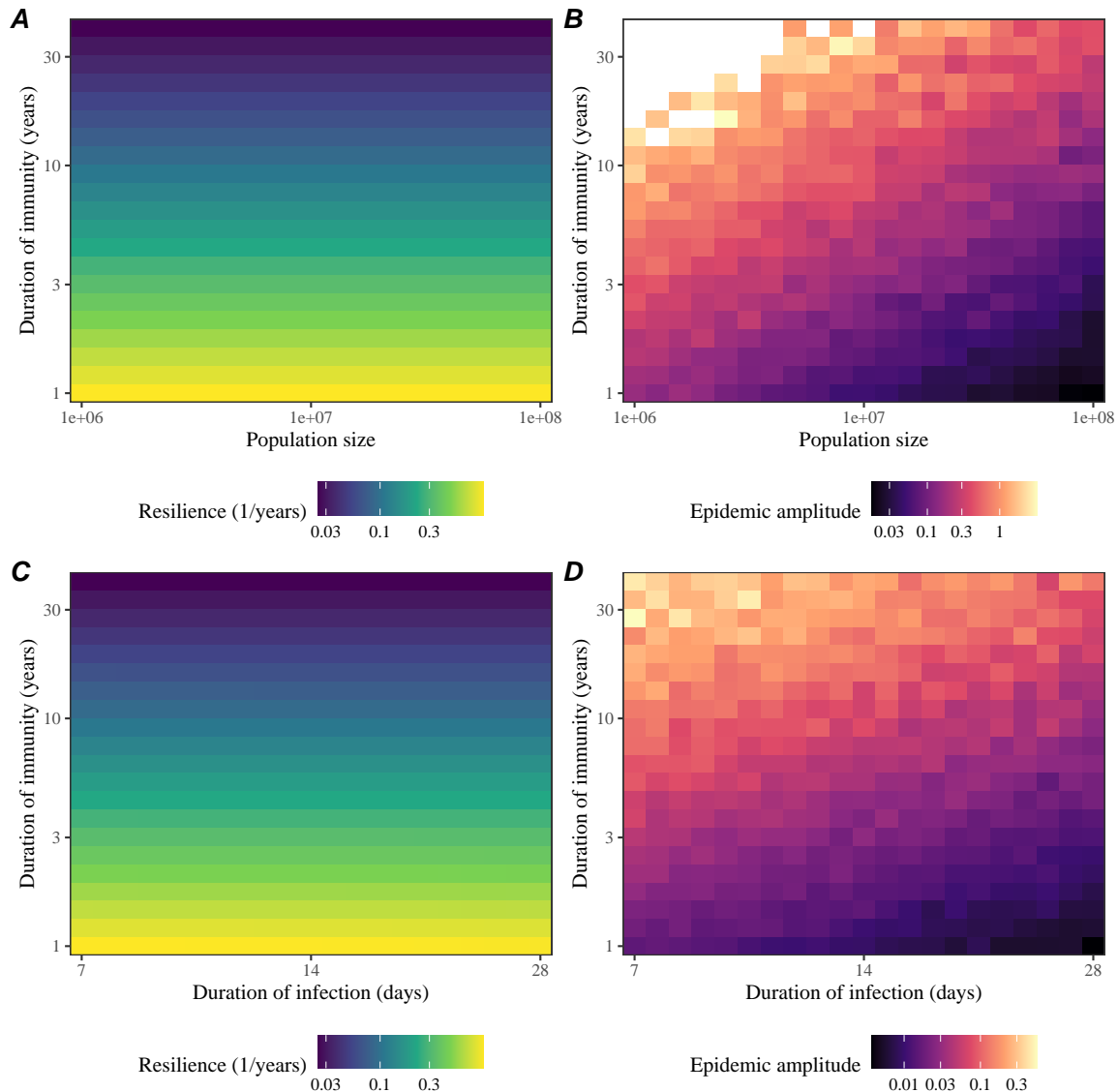


Figure S15: Impact of population size and the average duration of infection of a host-pathogen system on its sensitivity to stochastic perturbations. (A) Intrinsic resilience of a system as a function of population size and the average duration of immunity. (B) Epidemic amplitude as a function of population size and the average duration of immunity. (C) Intrinsic resilience of a system as a function of the average duration of infection and immunity. (D) Epidemic amplitude as a function of the average duration of infection and immunity. The epidemic amplitude corresponds to $(\max I - \min I)/(2\bar{I})$, where \bar{I} represents the mean prevalence.

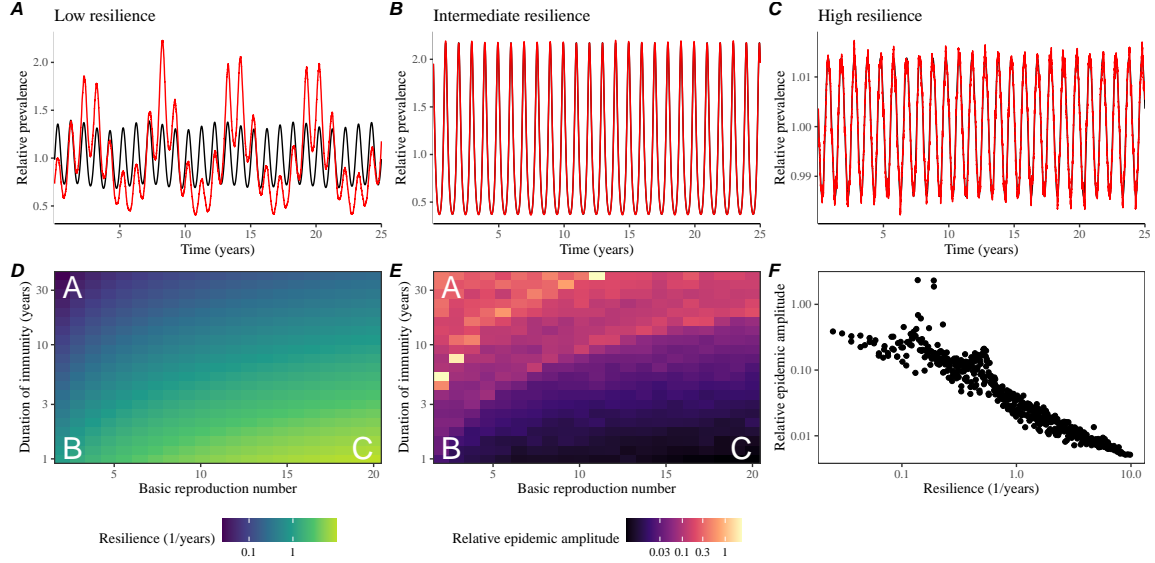


Figure S16: Linking resilience of a host-pathogen system to its sensitivity to stochastic perturbations for the seasonally forced SIRS model. (A–C) Epidemic trajectories of a stochastic SIRS model with demographic stochasticity across three different resilience values: low, intermediate, and high. The relative prevalence was calculated by dividing infection prevalence by its mean value. Black lines represent deterministic epidemic trajectories. Red lines represent stochastic epidemic trajectories. (D) The intrinsic resilience of the seasonally unforced system as a function of the basic reproduction number \mathcal{R}_0 and the duration of immunity. (E) The relative epidemic amplitude, a measure of sensitivity to stochastic perturbations, as a function of the basic reproduction number \mathcal{R}_0 and the duration of immunity. To calculate the relative epidemic amplitude, we first take the relative difference in infection prevalence between stochastic and deterministic trajectories: $\epsilon = (I_{\text{stoch}} - I_{\text{det}})/I_{\text{det}}$. Then, we calculate the difference between maximum and minimum of the relative difference and divide by half: $(\max \epsilon - \min \epsilon)/2$. Labels A–C in panels D and E correspond to scenarios shown in panels A–C. (F) The relationship between pathogen resilience and relative epidemic amplitude.

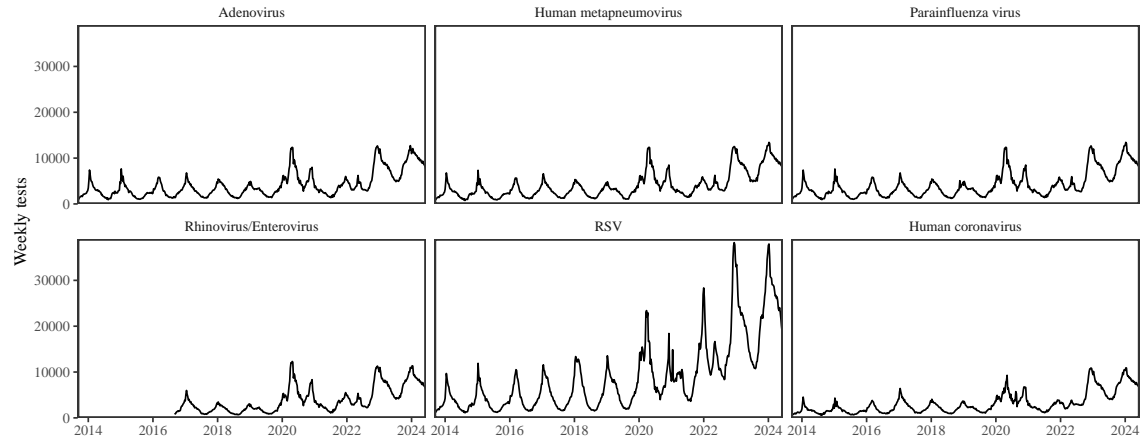


Figure S17: Testing patterns for respiratory pathogens in Canada.

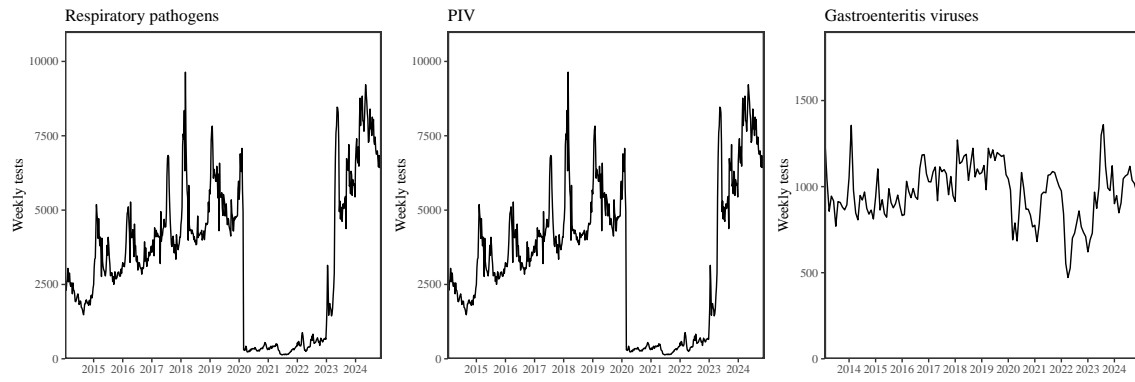


Figure S18: Testing patterns for respiratory pathogens, PIV, and gastroenteritis viruses in Hong Kong.

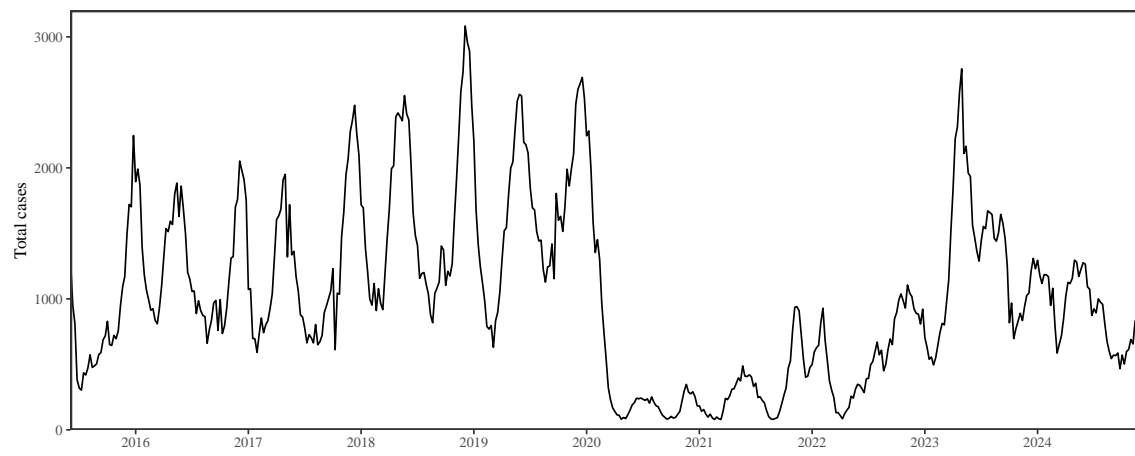


Figure S19: Total number of reported respiratory infection cases in Korea.

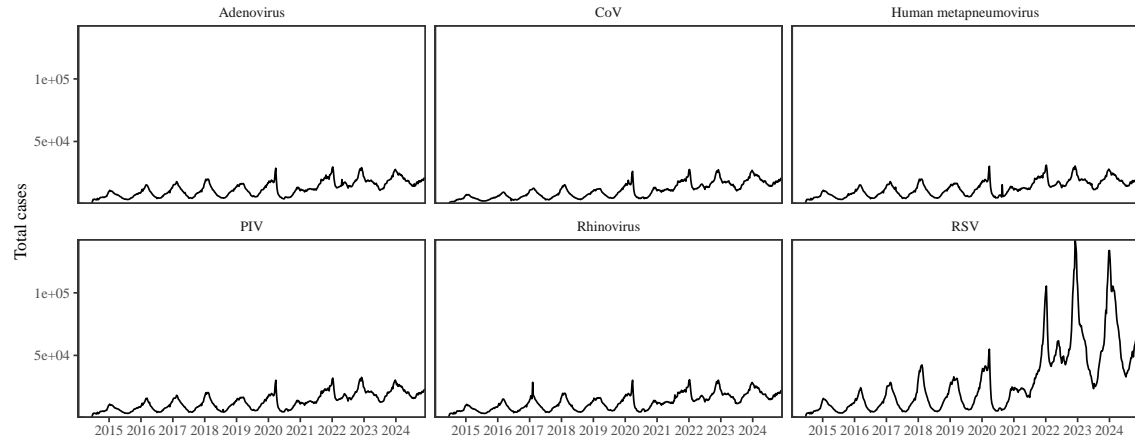


Figure S20: Testing patterns for respiratory pathogens in the US reported through the NREVSS.

837 **References**

- 838 [1] Rachel E Baker, Sang Woo Park, Wenchang Yang, Gabriel A Vecchi, C Jessica E
839 Metcalf, and Bryan T Grenfell. The impact of COVID-19 nonpharmaceutical
840 interventions on the future dynamics of endemic infections. *Proceedings of the*
841 *National Academy of Sciences*, 117(48):30547–30553, 2020.
- 842 [2] Gabriela B Gomez, Cedric Mahé, and Sandra S Chaves. Uncertain effects of the
843 pandemic on respiratory viruses. *Science*, 372(6546):1043–1044, 2021.
- 844 [3] Mihaly Koltai, Fabienne Krauer, David Hodgson, Edwin van Leeuwen, Marina
845 Treskova-Schwarzbach, Mark Jit, and Stefan Flasche. Determinants of RSV
846 epidemiology following suppression through pandemic contact restrictions. *Epi-*
847 *demics*, 40:100614, 2022.
- 848 [4] Sang Woo Park, Brooklyn Noble, Emily Howerton, Bjarke F Nielsen, Sarah
849 Lentz, Lilliam Ambroggio, Samuel Dominguez, Kevin Messacar, and Bryan T
850 Grenfell. Predicting the impact of non-pharmaceutical interventions against
851 COVID-19 on *Mycoplasma pneumoniae* in the United States. *Epidemics*,
852 49:100808, 2024.
- 853 [5] Amanda C Perofsky, Chelsea L Hansen, Roy Burstein, Shanda Boyle, Robin
854 Prentice, Cooper Marshall, David Reinhart, Ben Capodanno, Melissa Truong,
855 Kristen Schwabe-Fry, et al. Impacts of human mobility on the citywide trans-
856 mission dynamics of 18 respiratory viruses in pre-and post-COVID-19 pandemic
857 years. *Nature communications*, 15(1):4164, 2024.
- 858 [6] Eric J Chow, Timothy M Uyeki, and Helen Y Chu. The effects of the COVID-19
859 pandemic on community respiratory virus activity. *Nature Reviews Microbiol-*
860 *ogy*, 21(3):195–210, 2023.
- 861 [7] Stephen M Kissler, Christine Tedijanto, Edward Goldstein, Yonatan H Grad,
862 and Marc Lipsitch. Projecting the transmission dynamics of SARS-CoV-2
863 through the postpandemic period. *Science*, 368(6493):860–868, 2020.
- 864 [8] Rachel E Baker, Chadi M Saad-Roy, Sang Woo Park, Jeremy Farrar, C Jessica E
865 Metcalf, and Bryan T Grenfell. Long-term benefits of nonpharmaceutical inter-
866 ventions for endemic infections are shaped by respiratory pathogen dynamics.
867 *Proceedings of the National Academy of Sciences*, 119(49):e2208895119, 2022.
- 868 [9] Maaike C Swets, Clark D Russell, Ewen M Harrison, Annemarie B Docherty,
869 Nazir Lone, Michelle Girvan, Hayley E Hardwick, Leonardus G Visser, Pe-
870 ter JM Openshaw, Geert H Groeneveld, et al. SARS-CoV-2 co-infection with
871 influenza viruses, respiratory syncytial virus, or adenoviruses. *The Lancet*,
872 399(10334):1463–1464, 2022.

- 873 [10] Chun-Yang Lin, Joshua Wolf, David C Brice, Yilun Sun, Macauley Locke,
874 Sean Cherry, Ashley H Castellaw, Marie Wehenkel, Jeremy Chase Crawford,
875 Veronika I Zarnitsyna, et al. Pre-existing humoral immunity to human common
876 cold coronaviruses negatively impacts the protective SARS-CoV-2 antibody re-
877 sponse. *Cell host & microbe*, 30(1):83–96, 2022.
- 878 [11] Sam M Murray, Azim M Ansari, John Frater, Paul Klenerman, Susanna
879 Dunachie, Eleanor Barnes, and Ane Ogbe. The impact of pre-existing cross-
880 reactive immunity on SARS-CoV-2 infection and vaccine responses. *Nature*
881 *Reviews Immunology*, 23(5):304–316, 2023.
- 882 [12] John-Sebastian Eden, Chisha Sikazwe, Ruopeng Xie, Yi-Mo Deng, Sheena G
883 Sullivan, Alice Michie, Avram Levy, Elena Cutmore, Christopher C Blyth,
884 Philip N Britton, et al. Off-season RSV epidemics in Australia after easing
885 of COVID-19 restrictions. *Nature communications*, 13(1):2884, 2022.
- 886 [13] Stuart L Pimm. The structure of food webs. *Theoretical population biology*,
887 16(2):144–158, 1979.
- 888 [14] Michael G Neubert and Hal Caswell. Alternatives to resilience for measuring
889 the responses of ecological systems to perturbations. *Ecology*, 78(3):653–665,
890 1997.
- 891 [15] Lance H Gunderson. Ecological resilience—in theory and application. *Annual*
892 *review of ecology and systematics*, 31(1):425–439, 2000.
- 893 [16] Vasilis Dakos and Sonia Kéfi. Ecological resilience: what to measure and how.
894 *Environmental Research Letters*, 17(4):043003, 2022.
- 895 [17] Floris Takens. Detecting strange attractors in turbulence. In *Dynamical Sys-*
896 *tems and Turbulence, Warwick 1980: proceedings of a symposium held at the*
897 *University of Warwick 1979/80*, pages 366–381. Springer, 2006.
- 898 [18] Jonathan Dushoff, Joshua B Plotkin, Simon A Levin, and David JD Earn.
899 Dynamical resonance can account for seasonality of influenza epidemics. *Pro-*
900 , 101(48):16915–16916, 2004.
- 901 [19] Alan Hastings, Carole L Hom, Stephen Ellner, Peter Turchin, and H Charles J
902 Godfray. Chaos in ecology: is mother nature a strange attractor? *Annual review*
903 *of ecology and systematics*, pages 1–33, 1993.
- 904 [20] Alan Hastings, Karen C Abbott, Kim Cuddington, Tessa Francis, Gabriel Gell-
905 ner, Ying-Cheng Lai, Andrew Morozov, Sergei Petrovskii, Katherine Scran-
906 ton, and Mary Lou Zeeman. Transient phenomena in ecology. *Science*,
907 361(6406):eaat6412, 2018.

- 908 [21] Matthew B Kennel, Reggie Brown, and Henry DI Abarbanel. Determining
909 embedding dimension for phase-space reconstruction using a geometrical con-
910 struction. *Physical review A*, 45(6):3403, 1992.
- 911 [22] Eugene Tan, Shannon Algar, Débora Corrêa, Michael Small, Thomas Stemler,
912 and David Walker. Selecting embedding delays: An overview of embedding
913 techniques and a new method using persistent homology. *Chaos: An Interdis-*
914 *ciplinary Journal of Nonlinear Science*, 33(3), 2023.
- 915 [23] Bjarke Frost Nielsen, Sang Woo Park, Emily Howerton, Olivia Frost Lorentzen,
916 Mogens H Jensen, and Bryan T Grenfell. Complex multiannual cycles of My-
917 coplasma pneumoniae: persistence and the role of stochasticity. *arXiv*, 2025.
- 918 [24] Samantha Bosis, Susanna Esposito, HGM Niesters, GV Zuccotti, G Marseglia,
919 Marcello Lanari, Giovanna Zuin, C Pelucchi, ADME Osterhaus, and Nicola
920 Principi. Role of respiratory pathogens in infants hospitalized for a first episode
921 of wheezing and their impact on recurrences. *Clinical microbiology and infection*,
922 14(7):677–684, 2008.
- 923 [25] Miguel L O’Ryan, Yalda Lucero, Valeria Prado, María Elena Santolaya, Marcela
924 Rabello, Yanahara Solis, Daniela Berriós, Miguel A O’Ryan-Soriano, Hector
925 Cortés, and Nora Mamani. Symptomatic and asymptomatic rotavirus and
926 norovirus infections during infancy in a Chilean birth cohort. *The Pediatric
927 infectious disease journal*, 28(10):879–884, 2009.
- 928 [26] Virginia E Pitzer, Cécile Viboud, Vladimir J Alonso, Tanya Wilcox, C Jessica
929 Metcalf, Claudia A Steiner, Amber K Haynes, and Bryan T Grenfell. Environmental
930 drivers of the spatiotemporal dynamics of respiratory syncytial virus in
931 the United States. *PLoS pathogens*, 11(1):e1004591, 2015.
- 932 [27] Arthur WD Edridge, Joanna Kaczorowska, Alexis CR Hoste, Margreet Bakker,
933 Michelle Klein, Katherine Loens, Maarten F Jebbink, Amy Matser, Cormac M
934 Kinsella, Paloma Rueda, et al. Seasonal coronavirus protective immunity is
935 short-lasting. *Nature medicine*, 26(11):1691–1693, 2020.
- 936 [28] Jennifer M Radin, Anthony W Hawksworth, Peter E Kammerer, Melinda Bal-
937 ansay, Rema Raman, Suzanne P Lindsay, and Gary T Brice. Epidemiology
938 of pathogen-specific respiratory infections among three US populations. *PLoS
939 One*, 9(12):e114871, 2014.
- 940 [29] Guojian Lv, Limei Shi, Yi Liu, Xuecheng Sun, and Kai Mu. Epidemiological
941 characteristics of common respiratory pathogens in children. *Scientific Reports*,
942 14(1):16299, 2024.
- 943 [30] Saverio Caini, Adam Meijer, Marta C Nunes, Laetitia Henaff, Malaika Zounon,
944 Bronke Boudewijns, Marco Del Riccio, and John Paget. Probable extinction of

- 945 influenza b/yamagata and its public health implications: a systematic literature
946 review and assessment of global surveillance databases. *The Lancet Microbe*,
947 2024.
- 948 [31] Zhiyuan Chen, Joseph L-H Tsui, Bernardo Gutierrez, Simon Busch Moreno,
949 Louis du Plessis, Xiaowei Deng, Jun Cai, Sumali Bajaj, Marc A Suchard,
950 Oliver G Pybus, et al. COVID-19 pandemic interventions reshaped the global
951 dispersal of seasonal influenza viruses. *Science*, 386(6722):eadq3003, 2024.
- 952 [32] Hai Nguyen-Tran, Sang Woo Park, Kevin Messacar, Samuel R Dominguez,
953 Matthew R Vogt, Sallie Permar, Perdita Permaul, Michelle Hernandez, Daniel C
954 Douek, Adrian B McDermott, et al. Enterovirus D68: a test case for the use of
955 immunological surveillance to develop tools to mitigate the pandemic potential
956 of emerging pathogens. *The Lancet Microbe*, 3(2):e83–e85, 2022.
- 957 [33] Bryan T Grenfell, Ottar N Bjørnstad, and Bärbel F Finkenstädt. Dynamics of
958 measles epidemics: scaling noise, determinism, and predictability with the TSIR
959 model. *Ecological monographs*, 72(2):185–202, 2002.
- 960 [34] Samit Bhattacharyya, Per H Gesteland, Kent Korgenski, Ottar N Bjørnstad,
961 and Frederick R Adler. Cross-immunity between strains explains the dynamical
962 pattern of paramyxoviruses. *Proceedings of the National Academy of Sciences*,
963 112(43):13396–13400, 2015.
- 964 [35] Katharine R Dean, Fabienne Krauer, Lars Walløe, Ole Christian Lingjærde, Bar-
965 Barbara Bramanti, Nils Chr Stenseth, and Boris V Schmid. Human ectoparasites
966 and the spread of plague in Europe during the Second Pandemic. *Proceedings
967 of the National Academy of Sciences*, 115(6):1304–1309, 2018.
- 968 [36] Margarita Pons-Salort and Nicholas C Grassly. Serotype-specific immunity
969 explains the incidence of diseases caused by human enteroviruses. *Science*,
970 361(6404):800–803, 2018.
- 971 [37] Sarah Cobey and Edward B Baskerville. Limits to causal inference with state-
972 space reconstruction for infectious disease. *PloS one*, 11(12):e0169050, 2016.
- 973 [38] P Rohani, CJ Green, NB Mantilla-Beniers, and Bryan T Grenfell. Ecological
974 interference between fatal diseases. *Nature*, 422(6934):885–888, 2003.
- 975 [39] Sema Nickbakhsh, Colette Mair, Louise Matthews, Richard Reeve, Paul CD
976 Johnson, Fiona Thorburn, Beatrix Von Wissmann, Arlene Reynolds, James
977 McMenamin, Rory N Gunson, et al. Virus–virus interactions impact the popu-
978 lation dynamics of influenza and the common cold. *Proceedings of the National
979 Academy of Sciences*, 116(52):27142–27150, 2019.

- 980 [40] Neil Ferguson, Roy Anderson, and Sunetra Gupta. The effect of antibody-
981 dependent enhancement on the transmission dynamics and persistence of
982 multiple-strain pathogens. *Proceedings of the National Academy of Sciences*,
983 96(2):790–794, 1999.
- 984 [41] Public Health Agency of Canada. Respiratory virus detections in
985 Canada. 2024. <https://www.canada.ca/en/public-health/services/surveillance/respiratory-virus-detections-canada.html>. Accessed Sep
986 4, 2024.
- 988 [42] Centre for Health Protection. Detection of pathogens from respiratory spec-
989 imens. 2024. <https://www.chp.gov.hk/en/statistics/data/10/641/642/2274.html>. Accessed Nov 20, 2024.
- 991 [43] Centre for Health Protection. Detection of gastroenteritis viruses from faecal
992 specimens. 2024. <https://www.chp.gov.hk/en/statistics/data/10/641/717/3957.html>. Accessed Nov 20, 2024.
- 994 [44] Korea Disease Control and Prevention Agency. Acute respiratory infection,
995 Sentinel surveillance infectious diseases. 2024. <https://dportal.kdca.go.kr/pot/is/st/ari.do>. Accessed Nov 20, 2024.
- 997 [45] Edward Goldstein, Sarah Cobey, Saki Takahashi, Joel C Miller, and Marc Lipsitch.
998 Predicting the epidemic sizes of influenza A/H1N1, A/H3N2, and B: a
999 statistical method. *PLoS medicine*, 8(7):e1001051, 2011.
- 1000 [46] Karline Soetaert, Thomas Petzoldt, and R Woodrow Setzer. Solving differential
1001 equations in R: package deSolve. *Journal of statistical software*, 33:1–25, 2010.
- 1002 [47] R Core Team. *R: A Language and Environment for Statistical Computing*. R
1003 Foundation for Statistical Computing, Vienna, Austria, 2023.
- 1004 [48] Sang Woo Park, Inga Holmdahl, Emily Howerton, Wenchang Yang, Rachel E
1005 Baker, Gabriel A Vecchi, Sarah Cobey, C Jessica E Metcalf, and Bryan T Gren-
1006 fell. Interplay between climate, childhood mixing, and population-level suscep-
1007 tibility explains a sudden shift in RSV seasonality in Japan. *medRxiv*, pages
1008 2025–03, 2025.
- 1009 [49] Bob Carpenter, Andrew Gelman, Matthew D Hoffman, Daniel Lee, Ben
1010 Goodrich, Michael Betancourt, Marcus A Brubaker, Jiqiang Guo, Peter Li,
1011 and Allen Riddell. Stan: A probabilistic programming language. *Journal of
1012 statistical software*, 76, 2017.
- 1013 [50] Stan Development Team. RStan: the R interface to Stan, 2024. R package
1014 version 2.32.6.